





Article

The Discovery of the Romero VMS Deposit and Its Bearing on the Metallogenic Evolution of Hispaniola during the Cretaceous

Lisard Torró ^{1,2,3,*} , Joaquín A. Proenza ² , Julio Espailat ⁴, Albert Joan Belén-Manzeta ³, María Clara Román-Alday ², Alberto Amarante ⁴, Norverto González ⁴ , Jorge Espinoza ⁴, Manuel Jesús Román-Alpiste ⁵  and Carl E. Nelson ⁶

¹ Especialidad en Ingeniería Geológica, Facultad de Ciencias e Ingeniería, Pontificia Universidad Católica del Perú (PUCP), Av. Universitaria 180, San Miguel, Lima 15088, Peru

² Departament de Mineralogia, Petrologia i Geologia Aplicada, Universitat de Barcelona (UB), Martí i Franquès s/n, 08028 Barcelona, Spain; japroenza@ub.edu (J.A.P.); mariaclararoman@hotmail.com (M.C.R.-A.)

³ Universidad Tecnológica del Cibao Oriental (UTECO), Av. Universitaria s/n, Cotuí, Sánchez Ramírez 43000, Dominican Republic; albetbm3108@gmail.com

⁴ GoldQuest Mining Corp., 155 Wellington St. W Suite 2920, Toronto, ON M5V 3H1 Canada; julio.espailat@gmail.com (J.E.); jamarante@goldquestcorp.com (A.A.); norverto.gonzalez@gmail.com (N.G.); jespinoza@goldquestcorp.com (J.E.)

⁵ Instituto Andaluz de Ciencias de la Tierra, CSIC-Universidad de Granada, Av. de las Palmeras, 4, Armilla, 18100 Granada, Spain; mj.roman@csic.es

⁶ Recursos del Caribe, S.A., 2360 23rd Street, Boulder, CO 80304, USA; carlericnelson@gmail.com

* Correspondence: lisardtorro@hotmail.com; Tel.: +51-912-617-691

Received: 1 October 2018; Accepted: 2 November 2018; Published: 6 November 2018



Abstract: The recently discovered Romero deposit, located in the Tres Palmas district, Cordillera Central of the Dominican Republic, has probable reserves of 840,000 oz gold, 980,000 oz silver and 136 Mlb copper. Mineralization is hosted by intermediate volcanic and volcanoclastic rocks of the lower stratigraphic sequence of the Cretaceous Tiroo formation. The andesitic host rocks yield a U-Pb zircon concordia age of 116 ± 10 Ma. Au–Ag–Cu(–Zn) mineralization is divided into: (1) an upper domain with stacked massive sulfide lenses and sulfide dissemination within a 20-m-thick level of massive anhydrite-gypsum nodules, and (2) a lower domain with a high-grade stockwork mineralization in the form of cm-scale veins with open space fillings of fibrous silica and chalcopyrite, sphalerite, pyrite (+electrum \pm Au–Ag tellurides). The $\delta^{34}\text{S}$ values of sulfides from the upper (-7.6 and $+0.9\%$) and lower (-2.4 and $+5.6\%$) domains are consistent with a heterogeneous sourcing of S, probably combining inorganically and organically induced reduction of Albian-Aptian seawater sulfate. Despite this, a magmatic source for sulfur cannot be discarded. The $\delta^{34}\text{S}$ ($+19.2$ and $+20.0\%$) and $\delta^{18}\text{O}$ ($+12.5$ and $+14.2\%$) values of anhydrite-gypsum nodules are also consistent with a seawater sulfate source and suggest crystallization in equilibrium with aqueous sulfides at temperatures higher than 250 °C. These data point to a classification of Romero as a volcanogenic massive sulfide (VMS) deposit formed in an axial position of the Greater Antilles paleo-arc in connection with island arc tholeiitic magmatism during a steady-state subduction regime. Circulation of hydrothermal fluids could have been promoted by a local extensional tectonic regime expressed in the Tres Palmas district as a graben structure.

Keywords: VMS; Caribbean Greater Antilles; intra-oceanic island-arc; metallogenic evolution; Dominican Republic

1. Introduction

Exploration for gold and copper is currently being carried out in Early Cretaceous-to-Eocene age volcanic belts on Hispaniola, an island divided between the Dominican Republic and Haiti [1,2]. Arc-related rocks from the Cordillera Central of the Dominican Republic and its extension in the Massif du Nord in Haiti have been, and continue to be, the most intensively prospected. Current exploration follows previous sustained efforts from the 1970s that led to the discovery of the Cerro de Maimón volcanogenic massive sulfide (VMS) and the world-class Pueblo Viejo epithermal deposits, both of which are currently in production (Figure 1) [2–8]. The value of Dominican export of mineral resources in 2017 was US\$1766 M, of which gold was the main commodity with a value of US\$1456.7 M [9]. Haiti currently has no metallic mineral exports.

Economic and political stability, as well as an enviable mineral endowment, encouraged GoldQuest Mining Corp. to commence regional exploration of the most prospective areas of the Dominican Republic in 2001. After a stream sediment program revealed geochemical anomalies and mineralized outcrops on the southern side of the Cordillera Central, GoldQuest followed up with geologic mapping and sampling that led to the 2010 discovery, by diamond drilling, of the Romero South deposit containing approximately 300,000 ounces of gold [10]. Following ground geophysics (induced polarization (IP)), detailed geology and alteration mapping defined the highly prospective N–S Las Tres Palmas trend. Testing of the best targets led the company to the discovery of the Romero deposit (100% owned by GoldQuest and located about 165 km west-northwest of Santo Domingo, in the Province of San Juan) in 2012. Current indicated plus inferred resources for the two deposits (Romero plus Romero South) contain 1.93 Moz Au, 2.86 Moz Ag, 14.8 Mlbs Cu and 7.7 Mlbs Zn or 2.265 Moz gold equivalent [10]. A probable (mineable) reserve for the Romero deposit is 7.031 Mt @ 3.72 g/t Au, 4.33 g/t Ag and 0.88% Cu or 1.126 Moz. of gold equivalent [10].

Here, we present new data on the mineralogy, ore mineral texture and geochemistry, sulfur and oxygen isotopes for the Romero deposit, and a new U–Pb zircon age for the andesite host rock. These data are used to discuss the genesis of the Romero deposit and its classification, as well as the relative position of the mineralizing system within the metallogenic evolution of the Greater Antilles paleo-arc. The findings of this study have wider implications for the understanding of the occurrence of both VMS and porphyry-epithermal mineralization in single arc-related igneous terranes and their juxtaposition over evolution of these systems.

2. Geologic Setting

2.1. Geodynamic Setting

It is widely accepted that the modern Caribbean Plate is an allochthonous, Pacific Farallon-derived fragment, of which progressive west-to-east insertion into its current position was enabled by the Jurassic breakup of Pangea and the separation of the North America and Gondwana blocks [11,12]. Synchronous sea-floor spreading along the so-called Proto-Caribbean Seaway developed an intervening ocean basin that was progressively consumed along a west-directed subduction beneath the Caribbean (initially Farallon) Plate. Such subduction began as early as ca. 135 Ma along a sinistral inter-American transform fault connecting mature, east-dipping Cordilleran subduction zones along the western margins of North and South America [12,13]. Arc-continent collision along the northern leading edge of the Caribbean Plate in the latest Cretaceous-earliest Tertiary caused obduction of ophiolitic complexes onto continental margins in Guatemala, Cuba, Hispaniola and Puerto Rico [12,14–16]. On Hispaniola, subduction ceased after collision with the Bahamas Platform in the Eocene time [17,18]. Post-Eocene motion along the northern Caribbean Plate margin continues to be dominated by left-lateral strike-slip tectonics [19,20].

The Romero deposit is located in Central Hispaniola, on the southern side of the Cordillera Central of the Dominican Republic (Figure 1). The Cordillera Central is tectonically bounded by the left-lateral strike-slip, NNW–SEE to WNW–ESE trending Hispaniola and San Juan-Restauración fault

zones (represented by HFZ and SJRFZ, respectively, Figure 1). Geologically, it is a complex composite of crustal and mantle units that formed within an intra-oceanic environment since the Late Jurassic time and that accreted in the aftermath of the collision between the Caribbean island-arc and the Bahamas Platform in the Eocene time [21–23]. Rock units cropping out along the Central Cordillera are representative of (1) ultramafic, mostly serpentinized peridotites of probable Late Jurassic or Early Cretaceous protolith (including the so-called Loma Caribe peridotites [15,24,25]), (2) MORB-type volcano-plutonic assemblages representative of the Proto-Caribbean oceanic lithosphere (Loma la Monja assemblage [26]), (3) basaltic volcanic rocks of the Caribbean Large Igneous Province (CLIP, which comprises the plume-related Caribbean–Colombian Oceanic Plateau—CCOP), of the Jurassic to the latest Cretaceous age (Duarte complex and Pelona-Pico Duarte, Peña Blanca and Siete Cabezas formations [23,27–32]), and (4) igneous and sedimentary rocks associated with island arc(s) of Cretaceous age [33] (the corresponding units are described below). These basement rocks were variably deformed and metamorphosed [28,34–38], and are unconformably overlain by late Eocene to Holocene sedimentary rocks, which include siliciclastic and carbonate deposits.

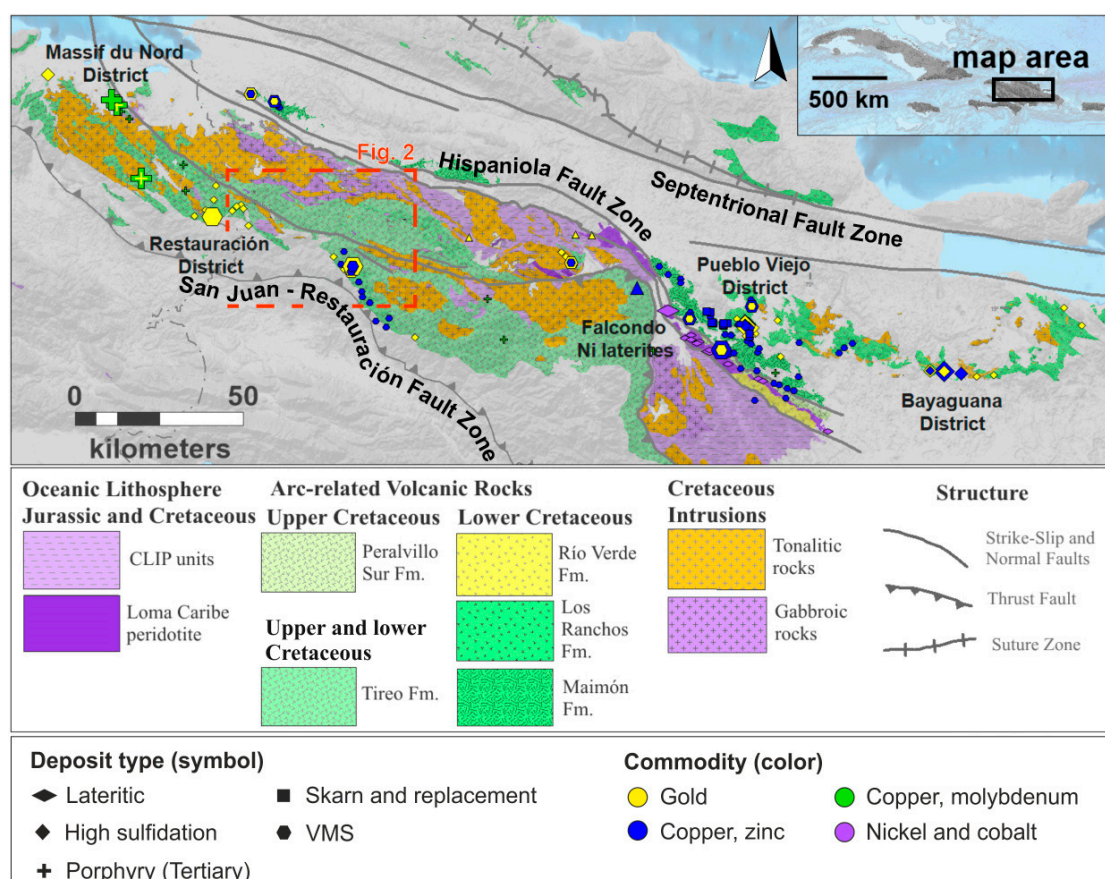


Figure 1. Geologic map of the Cordillera Central and Cordillera Oriental ranges in the Dominican Republic showing the main basement rock units. The geologic base map was modified from Nelson et al. [5]. The red box shows the location of the map in Figure 2.

Arc-related intrusive, volcanic and sedimentary units are bountifully exposed along the Cordillera Central. The Maimón formation, located in a median belt in the Bonao tectonic block [23,35], extends to the eastern limit of the Cordillera Central. Mafic-felsic, bimodal metavolcanic rocks of the Maimón formation, with forearc basalt (FAB), boninite and low-Ti island-arc tholeiite (IAT) signatures, record a lithogeochemical progression that is characteristic of subduction initiation ophiolites [37,39–41]. The age of the Maimón formation has been assigned to the Early Cretaceous based on U–Pb zircon dating [42] and their geochemical similitude to other arc-related rock units of the Early

Cretaceous age [6,33,38,40,41,43,44]. Thrust over the Maimón formation is the non-metamorphic Los Ranchos formation, which extends eastwards across the Dominican Cordillera Oriental and comprises mafic-felsic bimodal plutonic and volcanic series and volcanoclastic and terrigenous deposits. Igneous rocks from this geologic unit record archetypical geochemical progressions from subduction initiation to stable, mature subduction stages and embrace boninitic, low-Ti IAT, normal IAT and calc-alkaline signatures [7,8,22,45–47]. The age of the Los Ranchos formation has been constrained as Aptian-lower Albian, with U–Pb zircon ages determined between ca. 122 and 106 Ma [7,8,46,48,49]. The Maimón formation is separated from the Loma Caribe peridotite by the Peralvillo formation, a narrow sequence of undeformed and unmetamorphosed, arc-related volcanic and volcano-sedimentary rocks of the Late Cretaceous age [39,50] interpreted as evolved in a back-arc basin position [23]. To the south of the HFZ, on the southwest side of the median belt, crops out the Aptian-Albian Río Verde complex, composed of meta-igneous rocks with a weak subduction geochemical signature and proposed to be emplaced in a rifted arc or back-arc basin setting [51]. Finally, the arc-related Tiroo formation, first mapped by Bowin [52] and hosting the Romero deposit, crops out along most of high rugged mountains of the western Cordillera Central in the Dominican Republic and Massif du Nord in Haiti (Figure 1).

2.2. The Tiroo Formation

Rocks of the Tiroo formation [47] or group [23,53] and related units compose a more than 3-km-thick pile of arc-related volcanic and volcano-sedimentary sequences cropping out along a 290-km-long and 40-km-wide belt. In this article, we will refer to this geologic unit as a “formation” (in line with [47]). The volcanic pile is divided into a lower, mafic-dominated and an upper, felsic-dominated sequence [47,53]. The lower Tiroo volcanic sequence is largely composed of vitric–lithic tuffs and volcanic breccias of andesitic composition, which probably originated as pyroclastic deposits and were partially reworked as debris flows in a relatively deep submarine environment. However, accretionary lapilli levels deposited in shallow water transitional to a subaerial environment are described in SW Restauración (Figure 2) [47,53]. Interbedded with the dominant volcanoclastic levels are local massive basaltic flows and sedimentary rocks. The massive basalt flows are found towards the base of the lower volcanic sequence and are genetically associated with local microgabbros and dolerites [47]. Intercalation of discontinuous sedimentary strata occurs towards the base and the top of the lower volcanic sequence and includes cherts and limestones, of which the fossiliferous content allows bracketing the age of this volcanic sequence between the Aptian and Turonian times [53–55]. The upper volcanic sequence is composed mostly of lava flows, tuffs and tuff breccias of rhyolitic and dacitic composition deposited in a shallow submarine environment, the pyroclastic rocks being associated with phreatomagmatic activity [47]. The acidic deposits are interbedded with mafic flows and sediments, and the assemblage was intruded by dolerite dykes. Limestone lenses within the upper part of the upper volcanic sequence were dated at lower Senonian (i.e., broadly Coniacian–Santonian) in the Las Canitas area, and at early Maastrichtian to the east of Constanza [53]. In addition, radiolarians from a tuffaceous chert in the Pedro Brand section, northwest of Santo Domingo, indicate a Turonian–Coniacian age [32]. The coeval deposition of deep and shallow water pyroclastic rocks, the regional tectonics and the stratigraphic relationships with correlated units outside the main “Tiroo basin” led Lewis et al. [53] to propose rapid changes in the depth of the main basin in the framework of caldera collapse associated with a graben structure.

The chemical composition of the igneous rocks from the Tiroo formation was addressed by Escuder-Virueite et al. [47], who identified contrasting geochemical affinities along its igneous stratigraphy and proposed a major change in its magma sources. Basaltic and andesitic rocks of the lower volcanic sequence yield IAT signatures and were sourced by a mantle wedge fluxed with hydrous fluids expelled from the downgoing slab. In contrast, the mafic volcanic rocks interbedded within the upper volcanic sequence are identified as low-Ti, high-Mg andesites and Nb-enriched basalts. With regards to the felsic volcanic (and related intrusive sub-volcanic) rocks, these authors

identified transitional IAT to calc-alkaline as well as adakite affinities, with the former associated to deep partial melting of mafic rocks and the latter related to melts of the subducting slab.

Radiometric dating has been applied only to rocks of the upper volcanic sequence of the Tireo rocks and to rocks intruding the volcano-sedimentary pile. Published U–Pb zircon data include 91.3 ± 2.1 Ma [47] and 89.1 ± 0.9 Ma [23] ages for porphyric rhyolite flows of adakitic affinity from the lowermost levels of the upper volcanic sequence. On the other hand, a Nb-enriched andesitic dyke intruding the lower volcanic sequence was dated at 85.5 ± 2.6 Ma [47] and a gabbro intruding the Tireo formation in SW Villa Altagracia yields an age of 93.35 ± 0.23 Ma [23]. Whole-rock K/Ar dating of rhyolites (of unknown affinity) in the west of Valle Nuevo yield ages of 71.5 ± 3.6 and 85.1 ± 4.3 Ma, respectively [53]. Published hornblende $^{40}\text{Ar}/^{39}\text{Ar}$ plateau ages include 81.2 ± 8.2 Ma for a dacite sample [53], 91.8 ± 2.3 Ma for a rhyodacitic flow of adakitic affinity, 88.6 ± 1.8 Ma for a high-Mg andesitic dyke and 69.6 ± 0.7 Ma for a late biotite-bearing porphyritic andesite [47]. A plagioclase $^{40}\text{Ar}/^{39}\text{Ar}$ plateau age of 66.8 ± 0.47 Ma was obtained for a high-Mg porphyritic andesite flow [47].

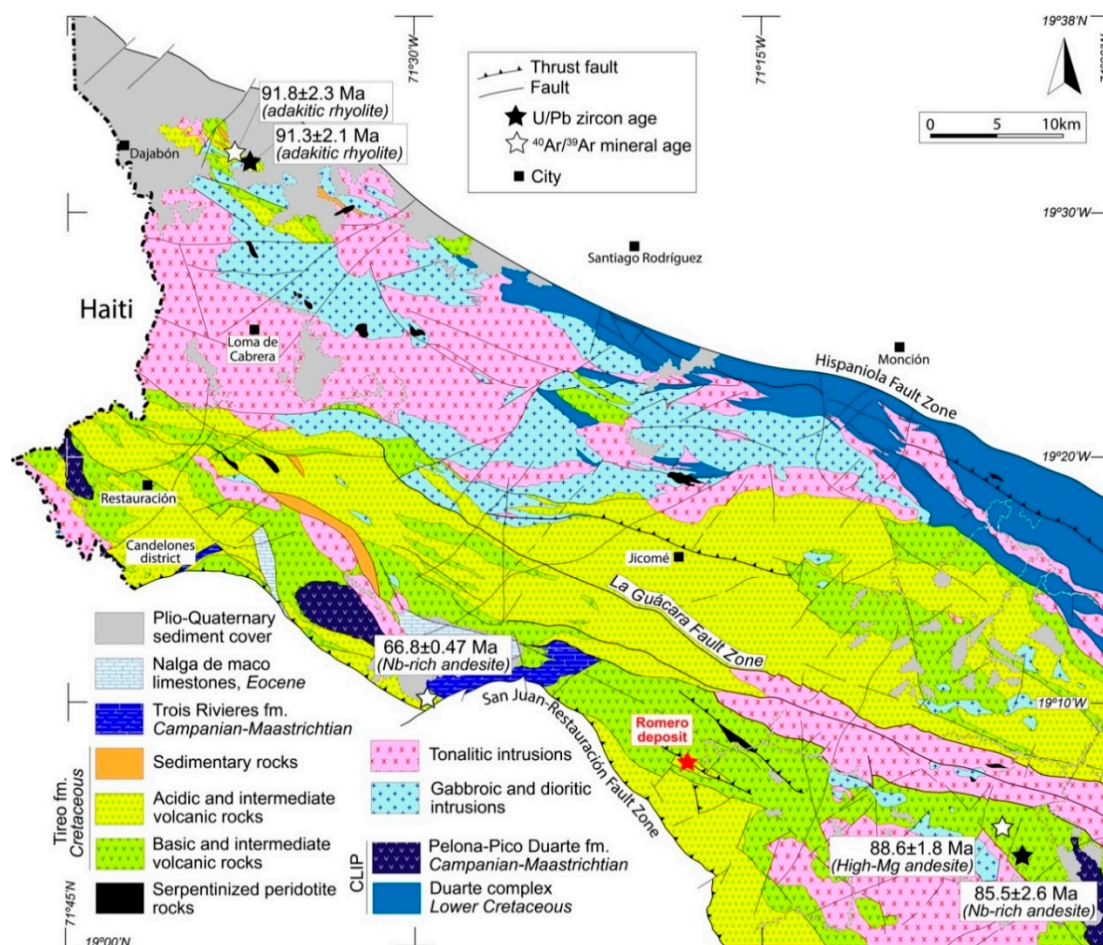


Figure 2. Geologic map of the NW Cordillera Central of the Dominican Republic showing the geologic units comprised fault zones between the Hispaniola and the San José-Restauración. The location of the Romero deposit is indicated with a red star. The U/Pb and $^{40}\text{Ar}/^{39}\text{Ar}$ ages are after Escuder-Viruete et al. [47].

3. Materials and Methods

This study was based on 112 drill core and in situ field samples collected from the Romero deposit and surroundings. Studied samples are representative of the different host rock lithofacies as well as the different mineralization features.

The samples were prepared as polished thick ($n = 26$) and thin ($n = 38$) sections for their study under the optical microscope using reflected and transmitted light. A selection of these samples was examined on an environmental scanning electron microscope (SEM) Quanta 200 FEI, XTE 325/D8395 equipped with an INCA Energy 250 EDS microanalysis system at Centres Científics i Tecnològics of the University of Barcelona (CCiT-UB) and on an environmental SEM Quanta 650 FEI, equipped with an EDAX-Octane Pro EDS microanalysis system at Centro de Caracterización de Materiales of the Pontifical Catholic University of Peru (CAM-PUCP). Operating conditions were an accelerating voltage of 20 keV and 5 nA in backscattered electron (BSE) mode. Mineral chemistry analyses of sulfide minerals were performed using a five-channel JEOL JXA-8230 electron microprobe (EMP) at the CCiT-UB, operated at a 20-kV acceleration voltage, a 20-nA beam current and with a beam diameter of 5 μm . Analytical standards and lines used for analyses were: sphalerite (Zn and S, $K\alpha$), chalcopyrite (Cu, $K\alpha$), FeS_2 (Fe, $K\alpha$), Au (Au, $M\alpha$), Ag (Ag, $L\alpha$), PbTe (Te, $L\alpha$), Sb (Sb, $L\alpha$), Bi (Bi, $M\alpha$), CdS (Cd, $L\alpha$), HgS (Hg, $M\beta$), PbS (Pb, $M\alpha$), GaAs (As, $L\alpha$), and ZnSe (Se, $L\alpha$).

Mineralogical determinations were also carried out by means of X-ray Diffraction (XRD; $n = 7$). The samples were ground in an agate mortar and were manually pressed by means of a glass plate to get a flat surface in cylindrical standard sample holders with a 16-mm diameter and a 2.5-mm height. The diffractograms were obtained in a X'Pert PRO MPD Alpha1 powder diffractometer (PANalytical, Almelo, The Netherlands) in Bragg-Brentano $\theta/2\theta$ geometry with a radius of 240 mm, nickel filtered Cu $K\alpha$ radiation ($k = 1.5418 \text{ \AA}$), and 45 kV–40 mA at the CCiT-UB. The software X'Pert Highscore © (Version 2.0.1, PANalytical, Almelo, The Netherlands) was used to subtract the background of the patterns, to detect the peaks and to assign mineral phases to each peak.

Zircons were separated from sample Romero-1 (a petrographic description for this rock is given below, and its whole rock composition is provided in Sheet-1 (Supplementary Materials)) at the University of Barcelona. The rock sample was crushed and milled using a tungsten carbide mill, and the resulting material was sieved (grain fractions: 125, 100, 75 and 40 μm) by means of disposable sieves in order to avoid contamination. Zircon crystals were separated using panning in water. Non-magnetic concentrates, after eliminating the magnetic fractions with a Frantz[®] isodynamic LB-1 separator, were processed by applying the hydroseparation technique (HS) at the HS-11 laboratory to obtain high-density mineral concentrates. The resulting non-magnetic high-density concentrates went through acid digestion in open bombs with combinations of HF, HCl and HNO_3 . Zircons were then handpicked under the binocular microscope and mounted in a 1-inch-diameter epoxy mount that was ground and polished to expose the grains. Photomicrograph maps and cathodoluminescence (CL) images were used to characterize the internal features of zircons such as growth zones and inclusions and to provide a base map for recording laser spot locations. For these images, a ZEISS EVO 15 SEM was used at the IACT-CSIC.

Zircon grains were analyzed for U–Th–Pb using a Cetac Photon Machines Analyte Excite 193 laser ablation system in conjunction with an Agilent 8800 QQQ inductively coupled plasma mass spectrometry (ICP-MS) in the IACT-CSIC. Fixed 20 μm -diameter spots were used with a laser frequency of 10 Hz and a fluence energy of 8 J/cm^2 . The ablated material was delivered to the torch by He and Ar gas. Instrument details, operation and acquisition parameters are given in Sheet-2 (Supplementary Materials).

Sulfur isotope analyses were carried out on 42 single sulfide grains and on 9 sulfate nodules from the different mineralization domains identified from the Romero deposit. Sulfide and sulfate minerals were separated by hand-picking techniques. Purity of the samples was tested by examination with a binocular microscope. The sorted material was then weighed in a tin capsule, adding V_2O_5 as an oxidizing catalyst. Isotopic ratios were obtained using a Delta C Finnigan MAT Delta-S mass spectrometer with an elemental analyzer at the CCiT-UB. For calibration, the international IAEA S3, IAEA S1, NBS-123 and IAEA S2 standards were used at the start and the end of every run. Oxygen isotope analyses were carried out on 5 sulfate grains. About 0.1 g of gypsum and anhydrite were dissolved in 50 mL of MilliQ water using stirring to accelerate the dissolution process. When the

solid phase was fully dissolved, sulfate was precipitated as BaSO_4 by the addition of excess BaCl_2 and acidifying the sample with HCl ($\text{pH} < 2$) and boiling it to prevent BaCO_3 precipitation. The precipitated BaSO_4 was then analyzed using the same equipment as for S isotope measurements. For calibration, the international NBS-127 and the internal YCEM ($\delta^{18}\text{O} = 17.6\text{‰}$) and BaSO_4 ($\delta^{18}\text{O} = 13.2\text{‰}$) standards were used. Sulfur and oxygen isotope compositions were expressed as the delta per mil (‰) values relative to the Canyon Diablo Troilite (CDT) and the Vienna-standard mean ocean water (V-SMOW) standards, respectively. Precision of the analyses was better than $\pm 0.2\text{‰}$. A table with the sulfur and oxygen isotope results is presented in Sheet-4 (Supplementary Materials).

4. Results

4.1. Petrography of the Hosting Rocks

Gold–silver–copper(–zinc) mineralization in the Romero prospect is hosted predominantly by volcanic and volcanoclastic rocks of intermediate and basic composition (Figure 3), which belong to the lower volcanic sequence of the Tiroo formation [47]. The descriptions and interpretations of the volcanic structures and textures below follow the guidelines of McPhie et al. [56]. Lithofacies identified in the host rocks include minor coherent lavas (Figure 4A) and more abundant volcanoclastic (Figure 4B–E) and volcanogenic sedimentary and/or pyroclastic (Figure 4F) deposits.

Coherent, massive lavas are of andesitic and rare dacitic composition, and show aphanitic, feldspar-, amphibole- and quartz-phyric textures, with a predominantly cryptocrystalline to glassy groundmass (Figure 4A,G). The phenocrysts range in size between 500 μm and 4 mm (Figure 4H,I) and form local monomineralic and polymineralic glomerules (Figure 4J). Plagioclase phenocrysts are by far more abundant than K-feldspar; these phenocrysts show euhedral and subhedral tabular habits and frequent compositional zoning, often picked out by selective alteration (Figure 4H) or by strings of melt inclusions. Quartz phenocrysts range from euhedral to anhedral, with the latter characterized by abundant embayment and voids infilled with the groundmass material (Figure 4G). Amphibole crystals are mostly euhedral (Figure 4I).

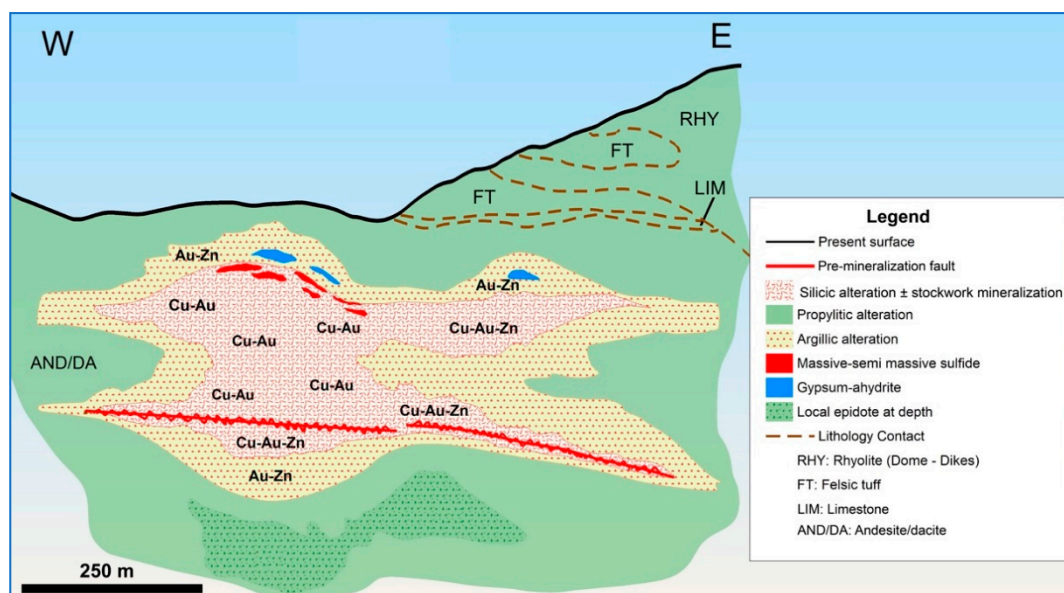


Figure 3. Schematic cross section showing the key geologic elements of the Romero deposit. Post-mineralization faults have been removed to facilitate the comprehension of the figure.

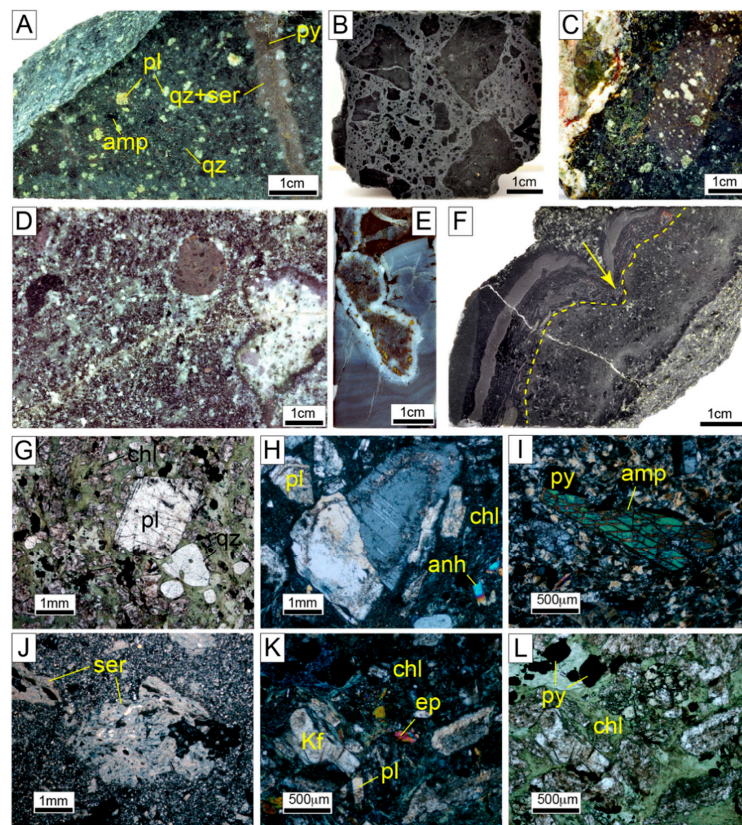


Figure 4. Hand sample photographs (A–F) and thin section photomicrographs (transmitted light, plain polarized light: (G,L); crossed polars: (H–K)) illustrating textures and mineralogy of the hosting volcanic, volcanoclastic and volcano-sedimentary rocks in the Romero deposit. (A) Andesite sample with a massive lithofacies and an aphanitic, porphyritic texture given by phenocrysts of plagioclase, amphibole and scarce quartz; (B) matrix-rich andesitic hyaloclastite with dark-rimmed vitriclasts showing curvilinear margins and depicting clast-in-matrix and local jigsaw-fit and tiny normal joints; (C) in this breccia of andesitic composition, all clasts show similar aphanitic, porphyritic and amygdaloidal textures; however, they have been variably silicified and chloritized, and as a result, their color is variable from clast to clast. The conspicuously irregular shapes and the monomict character of the clasts along with the poor sorting and the low proportion of matrix suggest that it is an autoclastic breccia; (D) in this matrix-rich breccia, rounded to sub-angular clasts of variable color are embedded in a crystal-rich matrix. Both the matrix and the clasts show extensive silicification; the relatively abundant crystal phenocrysts suggest a dacitic composition; (E) in this sample, interpreted as a peperite, islands of a pale green volcanic rock (magmatic component) crosscut the bedding of a silicified very-fine grained sedimentary rock; the volcanic component is wrapped by a white quartz rim enriched in pyrite and chalcocopyrite; (F) thin beds of gray mud (ash) alternate with beds of parallelly oriented, sand-sized black glass wisps. The bedding deforms around an andesitic angular clast some centimeters across, drawing a sag structure in which the most conspicuous aspects are the asymmetric folding of the gray mud layers and the thinning of the upper (in the sense indicated by the arrow) layer; (G) aphanitic, plagioclase- and quartz-phyric andesite, of which matrixes have been pervasively altered to chlorite; quartz phenocrysts show embayed margins and voids filled with the chloritized material of the groundmass; (H) zoned plagioclase crystals embedded in a fine grained, chloritized groundmass which also contains some small anhydrite crystals; (I) fresh amphibole phenocryst embedded in fine-grained groundmass composed of abundant plagioclase; (J) glomerule composed of tabular crystals pseudomorphically altered to sericite; (K) the porphyritic texture in this andesite is given by plagioclase and K-feldspar phenocrysts locally altered to sericite; the groundmass is pervasively altered to chlorite and epidote; (L) same image as in (K), in plane polarized light. Abbreviations: amp = amphibole; anh = anhydrite; chl = chlorite; ep = epidote; Kf = K-feldspar; pl = plagioclase; py = pyrite; qz = quartz; ser = sericite.

A variety of volcanoclastic lithofacies of andesitic and rare dacitic composition have been identified. They show a massive (non-bedded) arrangement. Monomict clast, vitriclast and shard-bearing breccias with abundant matrix and dominant jigsaw-fit and clast-in-matrix textures, displaying glassy rims in vitriclasts (Figure 4B), are interpreted as hyaloclastite deposits formed by in-situ quench fragmentation. On the other hand, monomict breccias characterized by a low proportion of matrix and irregularly shaped clasts lacking evidence of quenching (Figure 4C,D) are interpreted either as autoclastic breccias or as proximal resedimented clastic deposits, as they regularly contain clasts with curvilinear outlines and sharp edges. A further lithofacies observed along the volcanic sequence hosting the Romero deposit is characterized by thinly bedded mud layers of grey color and of silicic composition cut by lobate inclusions of a green aphanitic, aphyric material, which is thought to represent chloritized glass; the contact between these two materials is lined with white quartz (Figure 4E). Such rocks are interpreted as fluidal peperites.

Local bedded deposits are found incidentally within the volcanoclastic sequence described above. They are characterized by thin beds, up to 1.5 cm thick, of fine grained (mud-sized) sediments interspersed with layers rich in sandstone-sized particles (Figure 4F). Coarse elements within the latter include black glassy, chloritized components of chiefly cusped (shard-like) and blocky shapes. The conspicuous size selection and the occurrence of mudstones strongly suggest deposition from suspension, and hence either a pyroclastic fall-out or suspension associated with mass flows of volcanogenic origin is invoked. In the rock sample shown in Figure 4F, the bedding deforms around a blocky andesite clast, describing a sag structure, which is typically described in surge and fallout deposits; a detailed observation of the bright mudstone layer around the clast allows for the identification of asymmetrical folding probably developed by deformation of a wet sediment during the ballistic impact of the clast.

A ~25-m-thick discontinuous level containing abundant white and bright pink gypsum \pm anhydrite nodules is present in the upper sectors of the andesitic volcano-sedimentary sequence, topographically on top of stockwork mineralization (Figure 3). Such nodules are rounded and show intricate irregular outlines (Figure 5); they are compositionally very homogeneous, lacking mineral inclusions, and are cemented by an altered and mineralized volcanogenic sedimentary matrix containing glassy andesitic fragments.

Most of the studied host rock samples have pervasive quartz, chlorite \pm epidote (Figure 4G,L), or sericite (Figure 4J) alterations and dissemination of sulfides. The chlorite alteration is mostly developed on the recrystallized groundmass of lava flows or volcanoclastic deposits of andesitic composition, and is also observed pseudomorphically replacing crystals of mafic minerals. In contrast, sericite is observed as a replacement of plagioclase crystals, often along growth zones evidencing a primary compositional zoning of the feldspars. Disruption by faulting in the area precludes a clear identification of the distribution of the alteration types, but in general, widespread outer chlorite alteration passes inward to dominant sericite and finally to massive silicification in the stockwork zone (Figure 3).

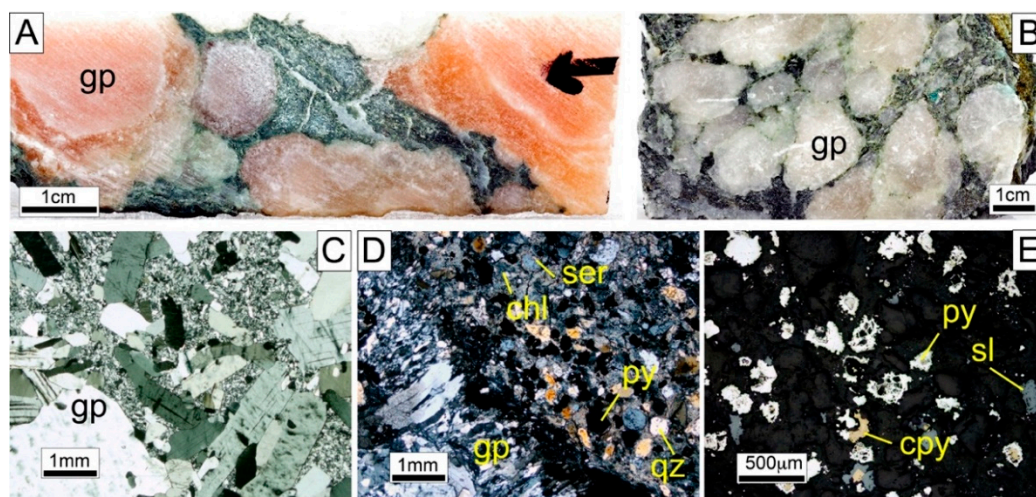


Figure 5. Hand sample photographs (A,B) and thin section photomicrographs (transmitted light, crossed polars: (C,D); reflected light: (E)) illustrating textures and mineralogy of the gypsum- and anhydrite-rich levels hosting disseminate mineralization atop the stockwork zone. (A,B) Pink and white cm-sized gypsum nodules are embedded in a green, fine-grained matrix; (C) massive aspect of a monomineralic gypsum nodule, formed by euhedral and subhedral mm-sized crystals in a fine-grained matrix; (D) detail of the contact between a gypsum nodule and the rock matrix, which is composed of crystals of anhydrite, quartz, plagioclase (altered to sericite), chlorite and a dissemination of sulfides; (E) pyrite is the most abundant sulfide mineral in the matrix of the gypsum-rich levels and appears as dissemination of cellular, framboidal and atoll-like crystals and grains along with sphalerite and chalcopyrite. Abbreviations: chl = chlorite; cpy = chalcopyrite; gp = gypsum; py = pyrite; qz = quartz; ser = sericite; sl = sphalerite.

4.2. U–Pb Geochronology

Zircons for U–Pb analyses were separated from an andesite autobreccia (sample Romero-1) composed of irregular clasts of aphanitic, highly plagioclase- and poorly amphibole- and quartz-phyric textures. This mineral composition and texture is shared by the scarce matrix surrounding the autoclasts to the point that their limits are often diffuse. The groundmass glassy material within the clasts and the matrix and the amphibole phenocrysts are pervasively altered to chlorite \pm epidote; in addition, the sample also shows intense silicification and a pyrite dissemination. Based on its immobile element composition (see data and related figures in Sheet-1 (Supplementary Materials), the rock is classified as andesite or andesitic basalt. The strong positive Th and negative Nb anomalies in the NMORB-normalized multi-elemental pattern points to a subduction-related origin for the sample [57] and are comparable to IAT basalts and basaltic andesites described by [47], as are the chondrite-normalized REE patterns.

The zircons separated from this rock are small, with lengths reaching around 50 μm , and their aspect ratios are in the range between 1 and 3. The bulk of the separated zircons yielded pre-Cretaceous ages, mostly around 300 Ma (not reported here) and hence are interpreted as inherited, xenocrystic grains. The relative abundance of inherited zircons in rocks from the Tiroe formation is also noted by Escuder-Virueite et al. [47]. For a state-of-the-art reading on the occurrence of inherited zircons in arc-related crust and mantle rocks in the Greater Antilles, the reader is referred to Torr o et al. [42], Rojas-Agramonte et al. [58] and Proenza et al. [59]. Only a 15% of the analyzed zircons yield Cretaceous ages ($n = 8$; see Sheet-2 (Supplementary Materials)) giving a concordia age at 116 ± 10 Ma (Figure 6). This Aptian-Albian age is interpreted as the crystallization age.

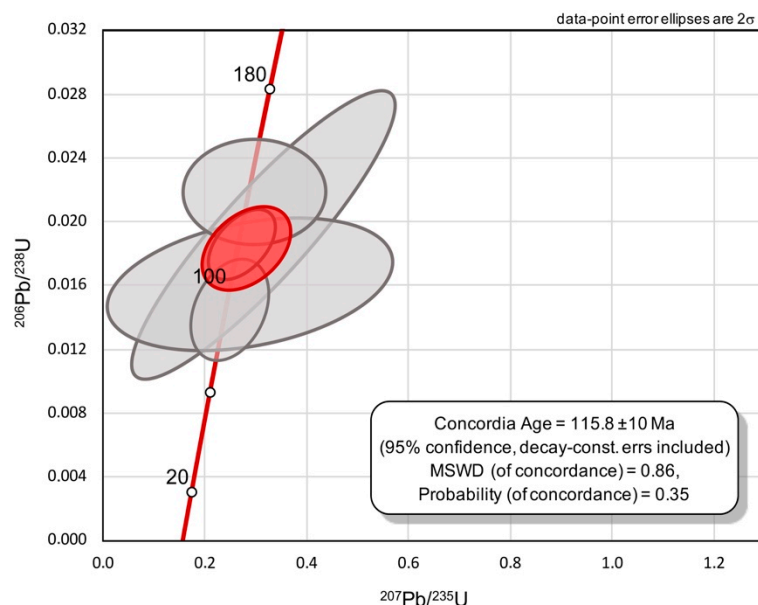


Figure 6. Concordia diagram for the andesitic rock hosting the Romero deposit ore. U–Pb procedures and analytical data are in Sheet-2 (Supplementary Materials).

4.3. Petrography of the Ore

High-grade mineralization of the Romero deposit occurs as vertically stacked, NE-dipping, sulfide lenses, some tens of meters thick, underlain by a dense vein stockwork (Figure 3). The main mineralization is located between 85 and 420 m below surface; its only expression at surface is in the form of very local, low-density, pyrite disseminations (further details on the geometry of the deposit are gathered in [10]).

In general terms, two domains of gold and associated base metal mineralization are identified. In the upper domain, mineralization occurs either as dissemination in the matrix around gypsum-anhydrite nodules or, more importantly, as massive sulfide bodies. The first one (up to 7.2 g/t Au, 23 g/t Ag, and 2% Zn) is composed of scattered sub-millimeter anhedral pyrite crystals, minor sphalerite and traces of chalcopyrite (Figure 5E). Pyrite grains show common anhedral morphologies including dendritic and branchy arrangements and is also observed as a replacement of micro-fauna shells, occasionally overgrowth by subhedral crystals depicting atoll-like structures.

In the massive sulfide bodies (up to 7.2 g/t Au, 63 g/t Ag, 12% Zn, and 5% Cu), macroscopic textures include massive, non-bedded homogeneous accumulations of sulfide minerals, as well as breccias composed in a large proportion of sub-angular massive sulfide clasts with sizes ranging from some tens of millimeters to some centimeters (Figure 7A). In the massive mineralization, the chalcopyrite and sphalerite are the most abundant minerals and appear cementing subhedral to anhedral pyrite grains with sizes mostly between 0.25 and 1 mm across (Figure 7B). Sphalerite hosts abundant micrometric blebs of chalcopyrite (chalcopyrite disease), and is replaced by chalcopyrite along its margins. The sulfide clasts show an equivalent mineralogy and texture (Figure 7C). Pyrite grains in the massive lenses show a wide variety of textures, including subhedral cubic crystals and complex textural features such as colloform overgrowths (Figure 7D,E), spongy cores rich in mineral inclusions (Figure 7F), spongy cellular cores (Figure 7G), micro-fauna shell replacement (Figure 7H), vermiculations, stalks, filaments, etc. Often, spongy cores are overgrowth by subhedral pyrite crystals drawing atoll-like textures. Framboidal (*sensu stricto*) textures in pyrite are not observed; however, spheroidal structures in the form of (putative) floriform textures are observed along growth bands in some pyrite grains (Figure 7E). The voids within pyrite grains are filled with gangue minerals (mostly quartz), chalcopyrite and lesser amounts of sphalerite and tennantite (Figure 7E).

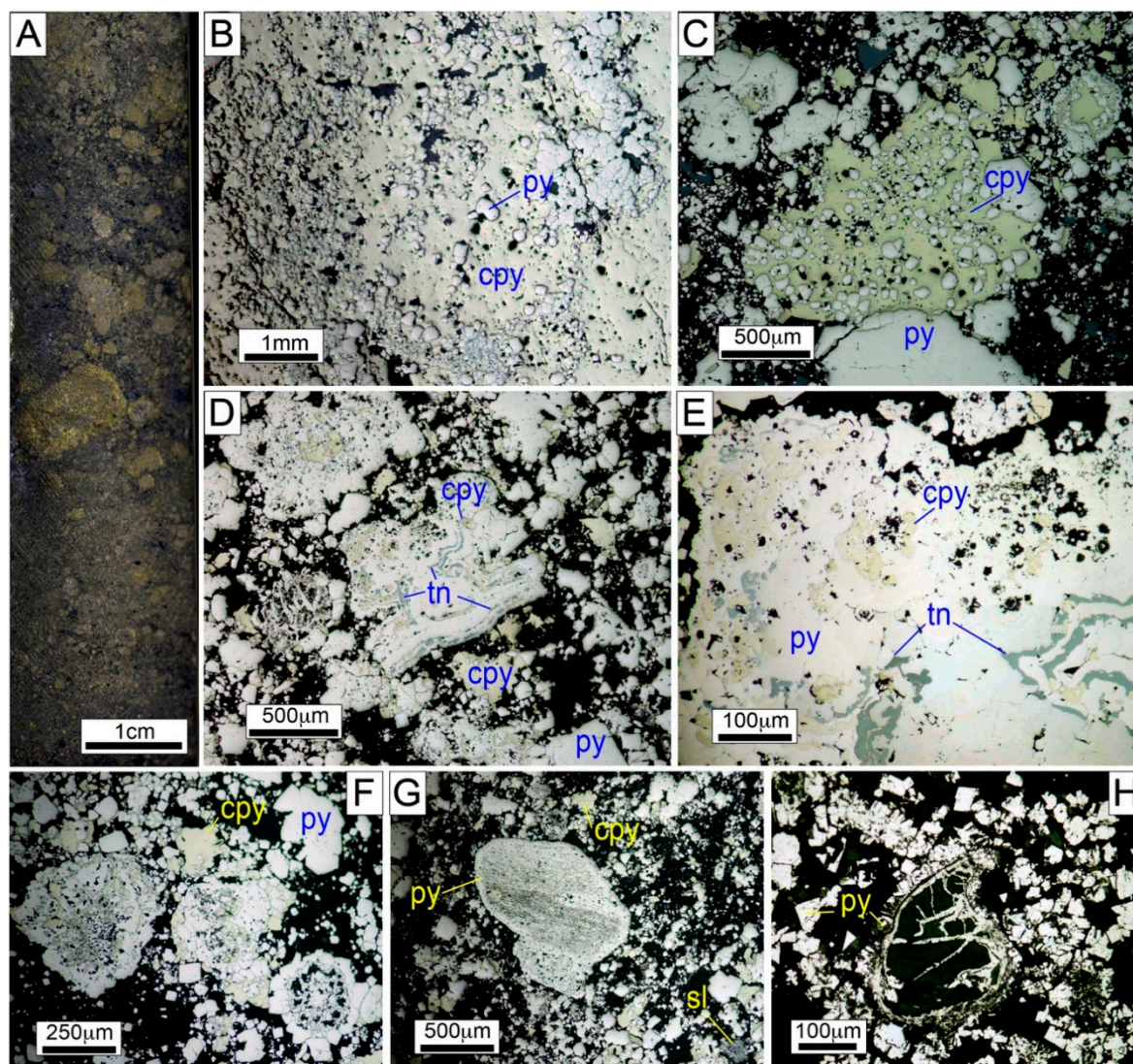


Figure 7. Hand sample photograph (A) and polished section photomicrographs (reflected light: B–H) illustrating textures and mineralogy of the massive sulfide mineralization at the Romero deposit. (A) Breccia composed of mm- to cm-sized massive sulfide clasts with sub-angular outlines; (B) sub-millimeter-sized anhedral pyrite grains in a chalcopyrite-rich groundmass; (C) detail of a chalcopyrite–pyrite clast pinched against a pyrite clast of a similar size; (D) detail of an anhedral, zoned pyrite grain with abundant chalcopyrite and tennantite infillings along vuggs distributed parallel to colloform growth faces; (E) detail of the tennantite and chalcopyrite lining vuggs in the pyrite grain shown in (D); note the irregular margins and the floriform, both radiating and concentric textures, probably corresponding to putative atoll structures, within the pyrite in the outer growth bands; (F) in these pyrite grains, a spongy, inclusion-rich core was overgrown by compact subhedral to euhedral pyrite crystals; the porosity is filled with gangue minerals (mostly quartz) and chalcopyrite; (G) pyrite grain with an inner spongy, cellular texture overgrowth by a thin layer of pristine pyrite; (H) micro-fauna shell replaced by pyrite included in a matrix rich in pyrite showing dendritic, branchy and spongy textures. Abbreviations: cpy = chalcopyrite; sl = sphalerite; tn = tennantite; py = pyrite.

The (lower) main Au–Ag–Cu(–Zn) zone (up to 288 g/t Au, 46 g/Ag, 13% Cu, and 10% Zn) comprises a 200-m-thick domain with a dense stockwork sulfide mineralization (Figures 8 and 9). Chalcopyrite- and gold-rich, centimeter-scale, sulfide-silica veins are conspicuous. Successive narrow subparallel layers of quartz of different colors and of sulfides (chalcopyrite + pyrite ± sphalerite) describe crustiform arrangements often with colloform and cockade textures (Figure 8A–E). On the

other hand, protrusions of chalcopyrite mineralization perpendicular to vein walls resemble comb textures (Figure 8B,E). Sphalerite, when present, is concentrated along the outer margins of the veins, and is overgrown by chalcopyrite and quartz bands towards the core of these structures (Figure 8D,E). In the veins, pyrite appears as subhedral grains up to 1 mm across, and shows fractures, engulfments and voids filled with chalcopyrite (Figure 8F,G) and lesser amounts of sphalerite. Sphalerite, showing local chalcopyrite disease, is crosscut by chalcopyrite veinlets (Figure 8G). Detailed observations under the microscope reveal a fibrous texture for the vein quartz, which on the other hand is free of fluid inclusions, suggesting recrystallization of chalcedony after silica gel deposition.

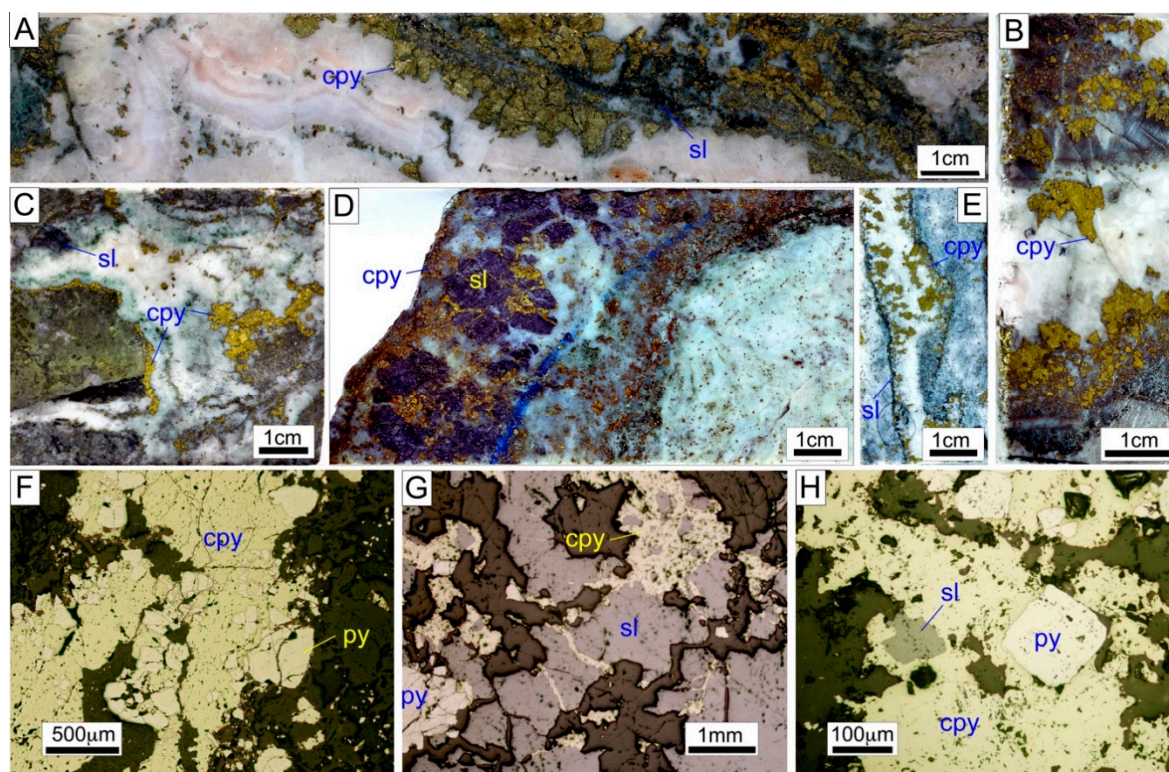


Figure 8. Hand sample photographs (A–E) and polished section photomicrographs (reflected light: F–H) illustrating textures and mineralogy of the stockwork mineralization at the Romero deposit. (A) In this sample, a colloform texture is described by quartz bands with different colors and crusts and bands enriched in sulfides; (B) detail of a quartz–sulfide vein in which chalcopyrite crystals located at its margins grew inward as protrusions perpendicular to the vein walls; (C) concentric bands of quartz and chalcopyrite grew away from a rock fragment describing a cockade texture; (D) cm-sized sphalerite crystals crosscut by chalcopyrite veinlets; (E) the margins of this vein are lined with sphalerite, which was overgrown by chalcopyrite protrusions; the remaining central space was filled with white quartz; (F) chalcopyrite cements anhedral pyrite grains; (G) detail of chalcopyrite veinlets crosscutting sphalerite mineralization; (H) chalcopyrite mineralization cements subhedral to anhedral pyrite crystals, fills vugs within these mineral and appears as very fine blebs within sphalerite (chalcopyrite disease). Abbreviations: cpy = chalcopyrite; sl = sphalerite; py = pyrite.

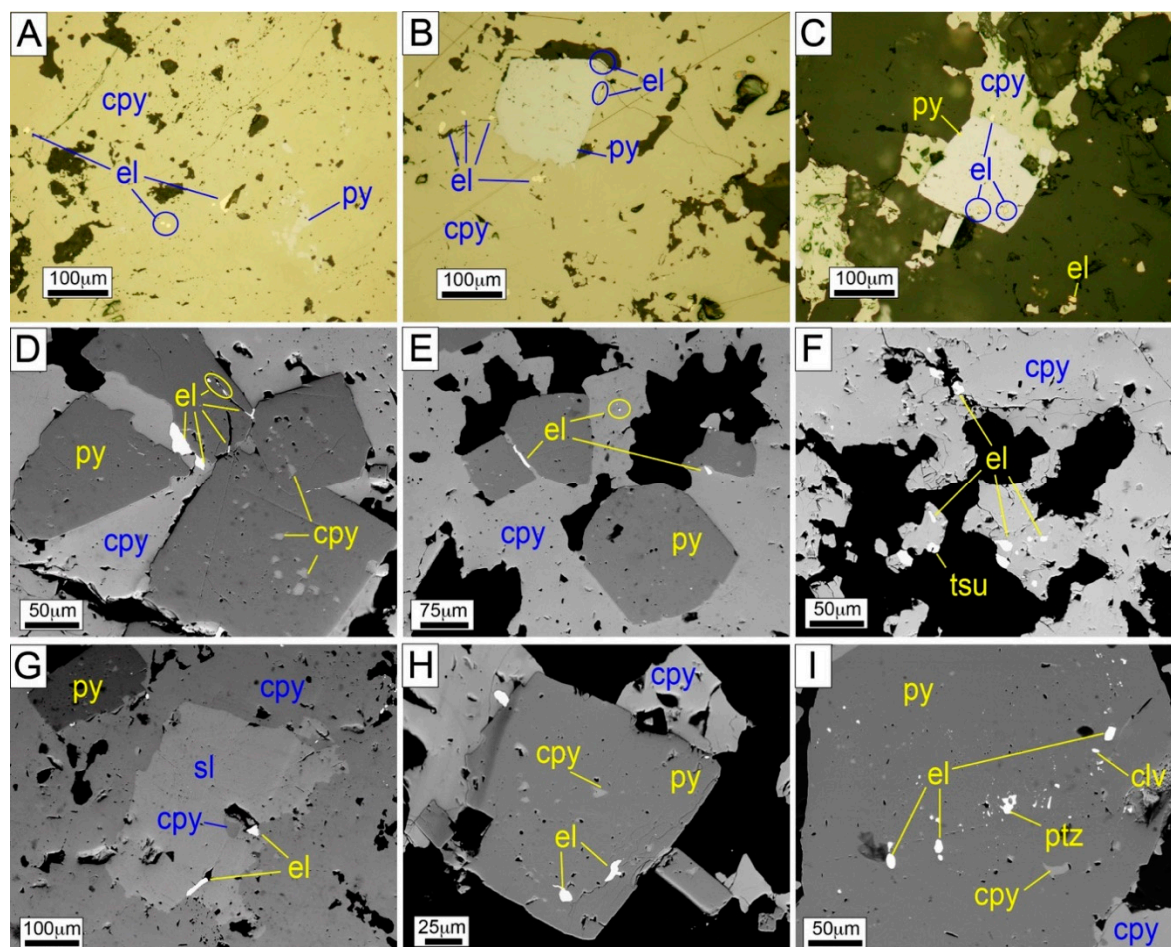


Figure 9. Thin section photomicrographs (reflected light: A–C) and SEM images (EDS mode: D–I) of electrum particles found in the Romero deposit lining vuggs in chalcopyrite (A,B,D–F), pyrite (C,D,H,I), and sphalerite (G) and in the gangue matrix (C). Abbreviations: clv = calaverite; cpy = chalcopyrite; el = electrum; sl = sphalerite; ptz = petzite; py = pyrite; tsu = tsumoite.

Electrum occurs largely in the stockwork mineralization in association with chalcopyrite (often lining vugs within this mineral) and concentrated along chalcopyrite–pyrite contacts (Figure 9A–F). Also abundant are the electrum particles included within pyrite grains, either as inclusion or lining vugs and fractures together with chalcopyrite (Figure 9C,H,I). Finally, some electrum is observed within quartz (Figure 9C) or sphalerite (Figure 9G). Electrum grains are some tens of microns across and very irregular in shape. A series of Bi–Au–Ag–tellurides of some tens of microns (mostly between 10 and 15 µm) across appear in the same textural positions as electrum, and include hessite (Ag_2Te), petzite (Ag_3AuTe_2), calaverite (AuTe_2) and tsumoite (BiTe ; Figure 9F,I).

The textural observations described above allow for the construction of a relatively simple paragenetic sequence shared by the mineralization in the upper (massive) and lower (stockwork) domains (Figure 10). Such paragenetic sequence includes an early precipitation of pyrite ($\pm\text{Au}$ rich electrum as inclusions; see mineral geochemistry below) followed by a stage rich in Zn (sphalerite) and a subsequent stage rich in Cu and Au (chalcopyrite, tennantite, electrum and tellurides).

Mineral	Formula	Pyrite stage	Zn stage	Cu+Au stage
Quartz (chalcedony)	SiO ₂			██████████
Pyrite	FeS ₂	██████████		
Sphalerite	ZnS		██████████	
Chalcocopyrite	CuFeS ₂			██████████
Tennantite	Cu ₆ [Cu ₄ (Fe,Zn) ₂]As ₄ S ₁₃			██████████
Electrum	(Au,Ag)	██████████		██████████
Hessite	Ag ₂ Te			██████████
Petzite	Ag ₃ AuTe ₂			██████████
Calaverite	AuTe ₂			██████████
Tsumoite	BiTe			██████████

Figure 10. Paragenetic sequence deduced for the mineralization in the Romero deposit. The width of the bars approximates the relative abundance of the listed minerals. Quartz (chalcedony) refers only to the occurrence of this mineral within the stockwork veins (lower zone). Hydrothermal alteration phases are not included in the table.

4.4. Ore Mineral Geochemistry

Analyzed electrum grains yield Au contents between 0.76 and 0.97 atoms per formula unit (a.p.f.u) and Ag contents between 0.03 and 0.24 a.p.f.u (Sheet-3, Supplementary Materials). The concentrations of other elements in electrum are conspicuously low and include Bi (up to 0.90 wt %, which is equivalent to 0.01 a.p.f.u.), Hg (0.16 wt %) and Pb (up to 0.11 wt %, although largely below the detection limit for this element). Two populations of electrum with contrasting Ag and Au concentrations have been identified (Figure 11A). The first one, which is Ag-rich (0.76–0.81 Au p.f.u., 0.19–0.24 Ag p.f.u.), is more abundant and occurs within chalcocopyrite, sphalerite and gangue and also lining vugs within pyrite, often along with chalcocopyrite. The second one has contrastingly lower Ag contents (0.91–0.97 Au p.f.u., 0.03–0.08 Ag p.f.u.) and has been observed only within pyrite as monomineralic inclusions.

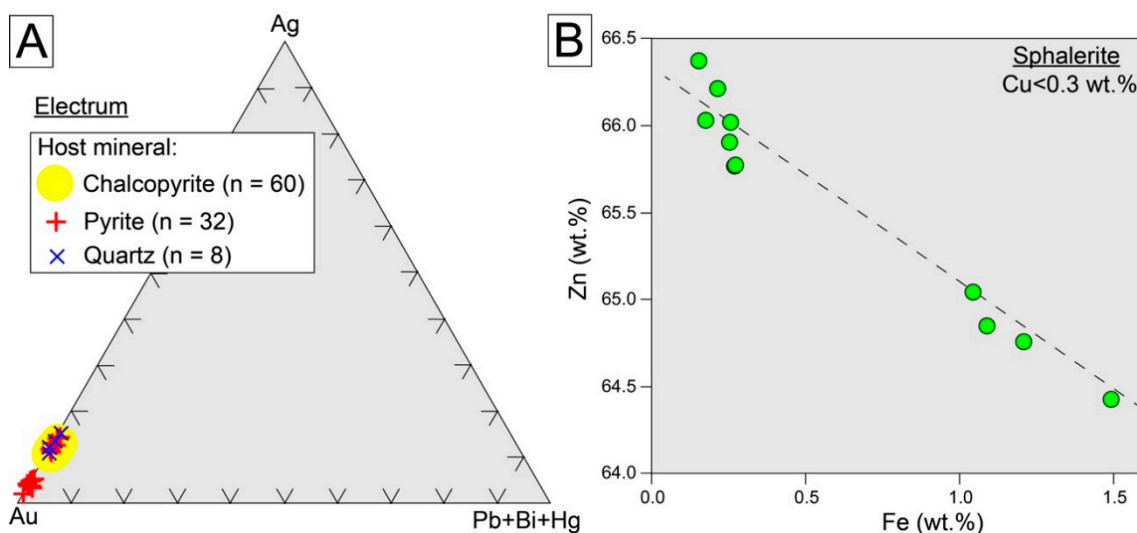


Figure 11. Chemical composition of electrum (A; Au–Ag–Pb + Bi + Hg ternary plot) and of sphalerite (B; Fe–Zn binary plot) analyzed from the Romero deposit. Concentrations are in wt % of the elements.

Analyzed sphalerite crystals yield a wide range of Cu contents from values below the detection limit to 6.36 wt %. Such enrichment in Cu strongly correlates with the concentrations of Fe (see Sheet-3, Supplementary Materials), indicating incidence of mixed sphalerite–chalcocopyrite analyses due to the common occurrence of micro-inclusions of chalcocopyrite within sphalerite, as described above.

Those analyses not affected by the chalcopyrite disease (threshold at Cu < 0.3 wt %; [6,60,61]) and hence preserving the primary compositions, have notably low Fe contents (up to 1.49 wt % or 0.03 a.p.f.u.), low Fe/Zn (<0.03) and S concentrations between 31.27 and 31.93 wt %. The negative correlation between Zn and Fe (Figure 11B) points to a substitution of Fe for Zn (e.g., [62]). Cadmium and mercury concentrations are as high as 0.35 and 0.59 wt %, respectively.

4.5. Sulfur and O Isotopes

In Romero samples, $\delta^{34}\text{S}$ values for the analyzed sulfides range between -7.6 and $+5.6\text{‰}$, with most of the values preferentially distributed around 0‰ (Figure 12). The $\delta^{34}\text{S}$ values of sulfides from the lower domain (stockwork mineralization) range between -2.4 and $+5.6\text{‰}$ ($+1.2$ to $+1.5\text{‰}$ for sphalerite, -1.7 to $+1.5\text{‰}$ for chalcopyrite and -2.4 to $+5.6\text{‰}$ for pyrite). Analyzed sulfide minerals from the upper mineralization domain yielded $\delta^{34}\text{S}$ values between -7.6 and $+0.9\text{‰}$, which are, in general, lower than those yielded by the studied sulfides from the stockwork mineralization (Figure 12). Within this range, $\delta^{34}\text{S}$ values span between -1.2 and -0.9‰ for chalcopyrite, between 0.0 and $+0.9\text{‰}$ for euhedral/compact pyrite grains, between -7.6 and $+0.4\text{‰}$ for spongy/shell replacement anhedral pyrite grains and -1.2‰ for a single analyzed sphalerite crystal. It is noteworthy that shell replacement pyrite (Figure 7H) yielded the lowest $\delta^{34}\text{S}$ values. The $\delta^{34}\text{S}$ values for the analyzed sulfates (anhydrite + gypsum) range between $+19.2$ and $+20.0\text{‰}$.

The $\delta^{18}\text{O}$ values for the analyzed sulfates are closely spaced between $+12.5$ and $+14.2\text{‰}$ (Figure 12).

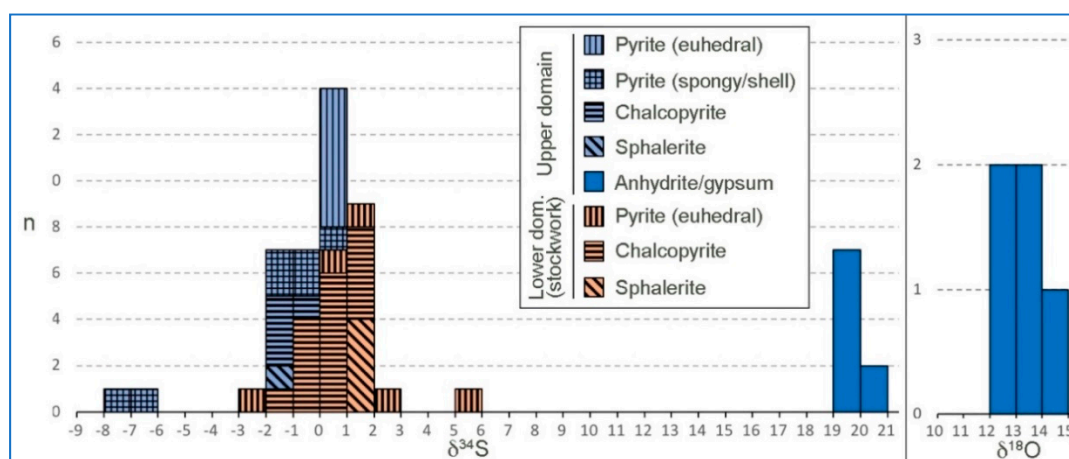


Figure 12. Histograms showing the range of sulfur (‰ , Canyon Diablo Troilite standard) and oxygen (Vienna-standard mean ocean water standard) isotope data for sulfides and sulfates from the Romero deposit.

5. Discussion

5.1. Classification of the Romero Deposit

In 2015, three years after the discovery of the Romero deposit, geotechnical drilling unexpectedly cut stacked lenses of massive sulfide. Prior to 2015, a lively debate over the origin and classification of this deposit existed among exploration geologists. This debate reflected a generalized uncertainty on the style of mineralization found and to be found in the Tiroo formation and the still poorly understood metallogenic evolution of this unit [3,63,64]. Currently, mineral exploration companies active in the Tiroo formation are preferentially targeting VMS (e.g., [65,66]).

The most prominent textural feature at the Romero deposit, and the first to be intersected by drilling is the high-grade stockwork mineralization (Figure 8). Open-space vein infillings with evidence of early amorphous and microcrystalline, fibrous silica precipitation could have misled early workers favoring an intermediate sulfidation epithermal mineralization style (e.g., [64]) despite the lack of clear

mineralogical evidence for this assignation (e.g., the outstanding predominance of chalcopyrite over sphalerite and the absence of diagnostic tennantite-tetrahedrite in the veins; cf. [67]). The presence of colloform, microcrystalline textures would, in any case, suggest the existence of silica-supersaturated conditions, resulting in rapid nucleation and precipitation during the deposition of the silica bands, probably associated to boiling processes (see [68]). However, this last point could not be asserted for the Romero vein mineralization due to the lack of fluid inclusions in translucent minerals.

The upper levels of the Romero mineralization system offer the best evidence for its origin as a VMS deposit. Thick anhydrite-gypsum nodule levels spatially correlated with conspicuous metal values and the self-defining stacked massive sulfide lenses are diagnostic features. The anhydrite-gypsum nodules are mineralogically very homogeneous and lack either sulfide or gangue mineral inclusions ruling out a dominantly replacement origin; an exhalative genesis and later sedimentary reworking are, in contrast, very plausible and supported by isotopic data as discussed below. Significant amounts of exhalative anhydrite-gypsum are characteristic of many submarine hydrothermal deposits on mid-ocean ridges and back-arc basins in the modern seafloor and in ancient Kuroko-type VMS deposits [69]. The $\delta^{18}\text{O}$ values for the analyzed sulfates agree with an Aptian-Albian seawater sulfate source according to the estimated uncertainty of the seawater isotopic variation of Claypool curve [70,71].

The $\delta^{34}\text{S}$ values for Romero sulfide minerals show a relatively wide distribution around a modal value of 0‰ with dissimilar values for sulfides from the lower (stockwork, biased towards more positive $\delta^{34}\text{S}$) and upper (biased towards more negative $\delta^{34}\text{S}$) mineralization domains (Figure 12). These observations suggest a heterogeneous source for sulfur, which in a VMS environment might typically embrace: (1) inorganic reduction of seawater sulfate; (2) magmatic sulfur, either from a direct contribution from a vapor-rich magmatic fluid or after leaching of the volcanic host rocks; and (3) sulfur from microbial activity in sediments by means of bacterial sulfate reduction [72–76]. For the Romero deposit, most $\delta^{34}\text{S}$ values (excluding the most negative ones, <6‰; Figure 12) can be explained either by an inorganic reduction of seawater sulfate or by a magmatic sulfur source. Even if an unambiguous discrimination between these two sources is not possible, it is noteworthy that an inorganic reduction of Aptian-Albian seawater sulfate (of which $\delta^{34}\text{S}$ was between ~15.3 and 16.6‰ [70,71]) would account for such a spectrum of $\delta^{34}\text{S}$ values and better explain the most positive values, as high as +5.6‰. The most negative $\delta^{34}\text{S}$ values, in sulfides from the upper mineralization zone, suggest a contribution of biogenically reduced sulfur, which is in good agreement with the biogenic textures described for sulfides in this domain (Figure 7). Finally, the $\delta^{34}\text{S}$ values of studied sulfate nodules are higher than those of Aptian-Albian seawater sulfate, which could point to seawater sulfate reduction at temperatures higher than 250 °C in equilibrium with aqueous sulfides (cf. [75]).

5.2. The Romero VMS Deposit within the Metallogenic Evolution of the Tiroo Formation

Volcano-sedimentary facies of the lower Tiroo formation, in which the Romero VMS deposit is hosted, indicate abrupt changes in the depth of deposition [53]. The referred workers contextualized such changes as the result of a locally extensional tectonic regime in the form of graben structure leading to caldera collapse and, back in 1991, already described it as “similar to Kuroko in Japan”. Certainly, extension might have played an important role during the circulation of hydrothermal fluids leading to the formation of VMS mineralization. Lithofacies and important petrogeochemistry of igneous rocks indicate, on the other hand, deposition of the sequence in an intra-oceanic island-arc scenario and, more specifically, in an axial arc position during Albian-Aptian times [47].

The Tiroo formation in the Dominican Republic and its continuation to the Massif du Nord in Haiti is known for hosting a variety of deposit typologies that include porphyry and epithermal as well as VMS deposits [3]. Porphyry and epithermal mineralization in the Tiroo formation are systematically hosted by rocks of the upper sequence and connected to calc-alkaline plutonic and volcanic rocks of the Late Cretaceous age. The high-sulfidation epithermal mineralization of the Au–Ag–Cu Restauración district is the most highlighted one in terms of reserves and include the Candelones deposit (5.27 Mt at

5.27 g/t Au and 0.35% Cu) and a number of smaller mineral occurrences [3,77–79]. Porphyry Cu–Au mineralization is described in the Massif du Nord and includes the Blondin and Douvray deposits along with other smaller occurrences [3,80]. Re–Os dating of molybdenite from the Douvray deposit (inferred resources of 624,834 tons Cu, 0.303 Moz Au, 6.805 Moz Ag and 4790 tons Mo) yielded an age of 93.3 ± 0.3 Ma [4], which is coeval, within analytical error, with rocks of adakitic affinity from the Tireo formation [47].

The Tireo formation, therefore, records not only a major change in the chemical affinity of arc magmas (cf. [47]) but also a major change in metallic mineralization styles from its lower to its upper volcano-sedimentary sequences. With new data in hand, we shall conclude that at least two different episodes of hypogene mineralization are recorded in this unit. A first mineralization event in the form of VMS deposition was associated to IAT magmas during steady-state subduction of the Proto-Caribbean Plate beneath the Caribbean Plate; such mineralization was apparently linked to local extensional tectonics in the form of caldera collapse that could promote the circulation of hydrothermal fluids during Albian-Aptian times. A second event is characterized by the occurrence of porphyry Cu (\pm Au \pm Mo) porphyry and epithermal mineralization connected to calc-alkaline magmatism during mature stages of the subduction and adakite-like felsic rocks associated to slab-window formation during the Late Cretaceous time.

5.3. The Romero Deposit in the Metallogenic Evolution of the Greater Antilles

As previously discussed, the Romero VMS deposit (and likely other new discoveries in the Tireo formation) formed in an axial position of the Caribbean intra-oceanic paleo-arc in Albian-Aptian times in connection with IAT magmas. Keeping to the most recent review on the metallogenic evolution of the Greater Antilles [3], the Romero deposit could be broadly correlated in time with bimodal mafic VMS deposits in Cuba and the Dominican Republic. However, the correlation is not that straightforward with regards to the relative position (axial vs. back vs. fore arc) and geodynamic setting of the mineralizing systems, as these authors traced the formation of such bimodal VMS deposits in a forearc position in connection to early magmas emplaced during a subduction initiation regime (cf. [81,82]). More recent studies on such VMS deposits hosted in the Early Cretaceous Los Pasos (Cuba), Maimón and Los Ranchos (the Dominican Republic) formations have strengthened the connection of the VMS deposits they host to a subduction initiation regime during the emplacement of forearc basalts and boninitic lavas [6,8,40]. We should hence conclude that the new VMS mineralization found in the Tireo formation, of which Romero is the highlighted representative, might deserve a separate group within the metallogenic evolution of the Greater Antilles, in which its position in an axial arc position is emphasized as a contrasting feature regarding most coeval VMS described in the region.

6. Conclusions

The results of this study have led to the following conclusions:

1. The newly discovered Romero deposit is hosted by volcanic and volcanoclastic rocks of the lower sequence of the Tireo formation, and a hosting andesite has been dated at 116 ± 10 Ma.
2. The hypogene mineralization can be subdivided into: (a) an upper mineralization domain, in the form of stacked massive sulfide lenses and sulfides in the matrix of stratigraphic levels hosting massive anhydrite-gypsum nodules, and (b) a lower, high-grade stockwork domain.
3. Ore mineralogy in both domains comprises an early crystallization of pyrite, followed by a stage rich in sphalerite and a further stage rich in Cu (chalcopyrite \pm tennantite) and Au–Ag (electrum \pm Au–Ag tellurides).
4. Sulphur and oxygen isotopes ratios on sulfide and sulfate minerals suggest that these elements were sourced by coeval seawater sulfate and that sulfate reduction was dominated by inorganic processes along with a variable contribution of biogenically reduced sulfur; nevertheless, a magmatic source cannot be ruled out.

- The Romero VMS mineralizing system operated in an axial arc position during steady-state subduction, connected to IAT magmatism and local extensional tectonics (caldera collapse). This geologic setting contrasts with the forearc position of most broadly synchronous VMS deposits in the Greater Antilles, which formed in a forearc position linked to a subduction-initiation regime.

Supplementary Materials: The following are available online at <http://www.mdpi.com/2075-163X/8/11/507/s1>, Sheet-1: Whole-rock geochemical analysis of the sample Romero-1, from which dated zircons were separated, and related figures; Sheet-2: U–Pb LA-ICP-MS data for spot analyses of zircon grains from the andesite host (sample Romero-1), Tíreo formation, the Dominican Republic; Sheet-3: EPMA analyses of ore minerals from the Romero deposit, the Dominican Republic; Sheet-4: Sulfur and oxygen isotope analyses for sulfide and sulfate minerals from the Romero deposit, the Dominican Republic.

Author Contributions: Conceptualization, L.T. and J.A.P.; fieldwork, L.T., J.A.P., J.E. (Julio Espailat), A.A., A.J.B.-M., N.G., J.E. (Jorge Espinoza); methodology, L.T., J.A.P., M.C.R.-A., A.J.B.-M., M.J.R.-A.; writing of the original draft preparation, L.T.; writing of review and editing, J.A., J.E. (Julio Espailat), C.E.N.

Funding: This research has been financially supported by the Spanish projects CGL2012-36263 and CGL2015-65824, the Dominican project 2014-1B4-132, the Catalan projects SGR 2014-1661 and 2007-707 and by Goldquest Mining Corp.

Acknowledgments: The help and hospitality extended by the staff of GoldQuest during sampling at the Hondo Valle camp are also gratefully acknowledged. We appreciate the technical support by José Fernandes (Centro de Caracterización de Materiales, Pontificia Universidad Católica del Perú) and Xavier Llovet (Centres Científics i Tecnològics, Universidad de Barcelona, CCiT-UB) during the acquisition of the SEM-EDS and EPMA data, respectively, and of Joaquim Perona (CCiT-UB) during the preparation of samples for O and S isotope analyses. Ruth Difo is thanked for her priceless help during rock processing for zircon separation.

Conflicts of Interest: The authors declare no conflicts of interest. The funders had no role in the design of the study; in the collection, analyses, or interpretation of data; in the writing of the manuscript, or in the decision to publish the results.

References

- Micklethwaite, K. Haiti and Dominican Republic: Gold Fever. Available online: <http://www.mining-journal.com/focus/special-reports/haiti-and-dominican-republic-gold-fever> (accessed on 9 September 2018).
- Redwood, S.D. La industria minera de la República Dominicana en 2017. *Geonoticias* **2017**, *15*, 24–31.
- Nelson, C.E.; Proenza, J.A.; Lewis, J.F.; López-Kramer, J. The metallogenic evolution of the Greater Antilles. *Geol. Acta* **2011**, *9*, 229–264.
- Nelson, C.E.; Stein, H.J.; Dominguez, H.; Carrasco, C.; Barrie, T.; Torró, L.; Proenza, J. Re-Os dating of molybdenite from the Pueblo Viejo (Au–Ag–Cu–Zn) and Douvray Cu–Au districts. *Econ. Geol.* **2015**, *110*, 1101–1110. [[CrossRef](#)]
- Nelson, C.; Iturralde-Vinent, M.; Proenza, J.; Draper, G.; Escuder-Viruete, J.; Garcia-Casco, A. Metallogenic Map of the Greater Antilles, Scale 1:1,000,000. 2015 Recursos del Caribe, S.A. Available online: www.cbmap.net (accessed on 9 September 2018).
- Torró, L.; Proenza, J.A.; Melgarejo, J.C.; Alfonso, P.; Farré de Pablo, J.; Colomer, J.M.; García-Casco, A.; Gubern, A.; Gallardo, E.; Cazañas, X.; et al. Mineralogy, geochemistry and sulfur isotope characterization of the Cerro de Maimón (Dominican Republic), San Fernando and Antonio (Cuba): Lower Cretaceous VMS deposits associated to the subduction initiation of the Proto-Caribbean lithosphere within a fore-arc. *Ore Geol. Rev.* **2016**, *72*, 794–817.
- Torró, L.; Camprubí, A.; Proenza, J.A.; León, P.; Stein, H.J.; Lewis, J.F.; Nelson, C.E.; Chavez, C.; Melgarejo, J.C. Re–Os and U–Pb geochronology of the Doña Amanda and Cerro Kiosko deposits, Bayaguana district, Dominican Republic: Looking down for the porphyry Cu–Mo roots of the Pueblo Viejo-type mineralization in the island-arc tholeiitic series of the Caribbean. *Econ. Geol.* **2017**, *112*, 829–853. [[CrossRef](#)]
- Torró, L.; Proenza, J.A.; Camprubí, A.; Nelson, C.E.; Domínguez, H.; Carrasco, C.; Melgarejo, J.C. Towards a unified genetic model for the Au–Ag–Cu Pueblo Viejo district, central Dominican Republic. *Ore Geol. Rev.* **2017**, *89*, 463–494. [[CrossRef](#)]
- Exportaciones Totales República Dominicana por Sectores 2010–2017, Banco Central de la República Dominicana. Available online: https://gdc.bancentral.gov.do/Common/public/estadisticas/sector-externo/documents/Exportaciones_Anuales_6.xls (accessed on 9 September 2018).

10. Macdonald, G.; Gopinathan, I.; McLeod, K.; Makarenko, M.; Pineau, M.; Hennesy, T.; San Martin, A.; Stone, D.; Castro, L.; Bocking, K.; et al. *NI 43-101 Pre-Feasibility Study Technical Report for the Romero Gold Prospect, Dominican Republic*; JDS Eenergy & Mining, Inc.: Toronto, ON, Canada, 2016. Available online: <https://www.goldquestcorp.com/images/projects/romero/technical-reports/technicalreport-nov2016-goldquestmining.pdf> (accessed on 9 September 2018).
11. Boschman, L.M.; van Hinsbergen, D.J.J.; Torsvik, T.H.; Spakman, W.; Pindell, J.L. Kinematic reconstruction of the Caribbean region since the Early Jurassic. *Earth-Sci. Rev.* **2014**, *138*, 102–136. [[CrossRef](#)]
12. Pindell, J.L.; Maresch, W.V.; Martens, U.; Stanek, K.P. The Greater Antillean Arc: Early Cretaceous origin and proposed relationship to Central American subduction mélanges: Implications for models of Caribbean evolution. *Int. Geol. Rev.* **2012**, *54*, 131–143. [[CrossRef](#)]
13. Cárdenas-Párraga, J.; Garcia-Casco, A.; Proenza, J.A.; Harlow, G.E.; Blanco-Quintero, I.F.; Lázaro, C.; Villanova-de-Benavent, C.; Núñez-Cambra, K. Trace-element geochemistry of transform-fault serpentinite in high-pressure subduction mélanges (eastern Cuba): Implications for subduction initiation. *Int. Geol. Rev.* **2017**, *59*, 2041–2064. [[CrossRef](#)]
14. Garcia-Casco, A.; Iturralde-Vinent, M.A.; Pindell, J. Latest Cretaceous collision-accretion between the Caribbean Plate and Caribéana: Origin of metamorphic terranes in the Greater Antilles. *Int. Geol. Rev.* **2008**, *50*, 781–809. [[CrossRef](#)]
15. Lewis, J.F.; Draper, G.; Proenza, J.A.; Espaillet, J.; Jiménez, J. Ophiolite-Related Ultramafic Rocks (Serpentinites) in the Caribbean Region: A Review of the Occurrence, Composition, Origin, Emplacement and Ni-Laterite Soil Formation. *Geol. Acta* **2006**, *4*, 237–263.
16. Solari, L.A.; Garcia-Casco, A.; Martens, U.; Lee, J.K.W.; Ortega-Rivera, A. Late Cretaceous subduction of the continental basement of the Maya block (Rabinal Granite, central Guatemala): Tectonic implications for the geodynamic evolution of Central America. *Geol. Soc. Am. Bull.* **2013**, *125*, 625–639. [[CrossRef](#)]
17. Donnelly, T.W.; Beets, D.; Carr, M.J.; Jackson, T.; Klaver, G.; Lewis, J.; Maury, R.; Schellenkens, H.; Smith, A.L.; Wadge, G.; et al. History and tectonic setting of Caribbean magmatism. In *The Caribbean Region. The Geology of North America*; Dengo, G., Case, J.E., Eds.; Geological Society of America: Boulder, CO, USA, 1990; Volume H, pp. 339–374, ISBN 9780813754567.
18. Mann, P.; Draper, G.; Lewis, J.F. An overview of the geologic and tectonic development of Española. In *Geologic and Tectonic Development of the North-America-Caribbean Plate Boundary in Española*; Mann, P., Draper, G., Lewis, J.F., Eds.; Geological Society of America: Boulder, CO, USA, 1991.
19. Vila, J.M.; Boisson, D.; Butterlin, J.; Feinburg, H.; Pubellier, M. Le complexe chaotique fini-éocène de Chouchou (Massif du Nord d’Haïti); un enregistrement du début des décrochements senestres nord-Caraïbes. *C.R. Acad. Sci.* **1987**, *304*, 39–42.
20. Mann, P.; Calais, E.; Ruegg, J.C.; DeMets, C.; Jansma, P.E.; Mattioli, G.S. Oblique collision in the northeastern Caribbean from GPS measurements and geological observations. *Tectonics* **2002**, *21*, 1057. [[CrossRef](#)]
21. Lewis, J.F.; Draper, G. Geology and tectonic evolution of the Northern Caribbean margin. In *The Caribbean Region*; Dengo, G., Case, J.E., Eds.; Geological Society of America: Boulder, CO, USA, 1991; pp. 77–140.
22. Lewis, J.F.; Escuder-Viruete, J.; Hernaiz Huerta, P.P.; Gutiérrez, G.; Draper, G.; Pérez-Estaún, A. Geochemical subdivision of the Circum-Caribbean Island Arc, Dominican Cordillera Central: Implications for crustal formation, accretion and growth within an intra-oceanic setting. *Acta Geol. Hisp.* **2002**, *37*, 81–122.
23. Escuder-Viruete, J.; Joubert, M.; Urien, P.; Friedman, R.; Weis, D.; Ullrich, T.; Pérez-Estaún, A. Caribbean island-arc rifting and back-arc basin development in the Late Cretaceous: Geochemical, isotopic and geochronological evidence from Central Hispaniola. *Lithos* **2008**, *104*, 378–404. [[CrossRef](#)]
24. Proenza, J.A.; Zaccarini, F.; Lewis, J.F.; Longo, F.; Garuti, G. Chromian spinel composition and the platinum-group minerals of the PGE-rich Loma Peguera Chromitites, Loma Caribe peridotite, Dominican Republic. *Can. Mineral.* **2007**, *45*, 631–648. [[CrossRef](#)]
25. Marchesi, C.; Garrido, C.J.; Proenza, J.A.; Hidas, K.; Varas-Reus, M.I.; Butjosa, L.; Lewis, J.F. Geochemical record of subduction initiation in the sub-arc mantle: Insights from the Loma Caribe peridotite (Dominican Republic). *Lithos* **2016**, *252–253*, 1–15. [[CrossRef](#)]
26. Escuder-Viruete, J.; Pérez-Estaún, A.; Weis, D. Geochemical constraints on the origin of the late Jurassic proto-Caribbean oceanic crust in Hispaniola. *Int. J. Earth Sci.* **2009**, *98*, 407–425. [[CrossRef](#)]

27. Draper, G.; Lewis, J.F. Petrology and structural development of the Duarte complex, central Dominican Republic: A preliminary account and some tectonic implications. In Proceedings of the 10th Caribbean Geological Conference, Cartagena, Colombia, 15–19 August 1983; pp. 103–112.
28. Draper, G.; Lewis, J.F. Metamorphic belts in central Hispaniola. In *Geologic and Tectonic Development of the North American—Caribbean Plate Boundary in Hispaniola*; Mann, P., Draper, G., Lewis, J.F., Eds.; Geological Society of America: Boulder, CO, USA, 1991; pp. 29–46.
29. Kerr, A.C.; White, R.V.; Thompson, P.M.E.; Tarney, J.; Saunders, A.D. No oceanic plateau-No Caribbean Plate? The seminal role of an oceanic plateau in Caribbean Plate evolution. In *The Circum-Gulf of Mexico and Caribbean Region: Hydrocarbon Habitats, Basin Formation and Plate Tectonics*; Bartolini, C., Buffler, R.T., Blickwede, J.F., Eds.; American Association of Petroleum Geologists Memoir: Tulsa, OK, USA, 2003; pp. 126–168.
30. Escuder-Virueite, J.; Perez-Estaun, A.; Contreras, F.; Joubert, M.; Weis, D.; Ullrich, T.; Spades, P. Plume mantle source heterogeneity through time: Insights from the Duarte complex, Hispaniola, northeastern Caribbean. *J. Geophys. Res.* **2007**, *112*, B04203. [[CrossRef](#)]
31. Escuder-Virueite, J.; Perez-Estaun, A.; Joubert, M.; Weis, D. The Pelona–Pico Duarte basalts formation, central Hispaniola: An on-land section of Late Cretaceous volcanism related to the Caribbean large igneous province. *Geol. Acta* **2011**, *9*, 307–328.
32. Sandoval, M.I.; Baumgartner, P.O.; Escuder Viruete, J.; Gabites, J.; Mercier de Lepinay, B. Late Cretaceous radiolarian biochronology of the Pedro Brand section, Tíreo Group, eastern Central Cordillera, Dominican Republic: A contribution to the stratigraphy of the Caribbean Large Igneous Province. *Revue de Micropaléontologie* **2015**, *58*, 85–106. [[CrossRef](#)]
33. Lidiak, E.G.; Anderson, T.H. Evolution of the Caribbean plate and origin of the Gulf of Mexico in light of plate motions accommodated by strike-slip faulting. In *Late Jurassic Margin of Laurasia—A Record of Faulting Accommodating Plate Rotation*; Anderson, T.H., Didenko, A.N., Johnson, C.L., Khanchuk, A.I., MacDonald, J.H., Jr., Eds.; Geological Society of America: Boulder, CO, USA, 2015.
34. Nagle, F. Blueschist, eclogite, paired metamorphic belts, and the early tectonic history of Hispaniola. *Geol. Soc. Am. Bull.* **1974**, *85*, 1461–1466. [[CrossRef](#)]
35. Draper, G.; Gutiérrez, G.; Lewis, J. Thrust emplacement of the Hispaniola peridotite belt: Orogenic expression of the mid-Cretaceous Caribbean arc polarity reversal? *Geology* **1996**, *24*, 1143–1146. [[CrossRef](#)]
36. Escuder-Virueite, J.; Hernaiz-Huerta, P.P.; Draper, G.; Gutiérrez, G.; Lewis, J.F.; Pérez-Estaun, A. Metamorfismo y estructura de la Formación Maimón y los Complejos Duarte y Río Verde, Cordillera Central Dominicana: Implicaciones en la estructura y evolución del primitivo Arco-Isla Caribeño. *Acta Geol. Hispan.* **2002**, *37*, 123–162.
37. Escuder-Virueite, J.; Contreras, F.; Joubert, M.; Urien, P.; Stein, G.; Weis, D.; Pérez-Estaun, A. Tectónica y geoquímica de la Formación Amina: Registro del arco isla Caribeño primitivo en la Cordillera Central, República Dominicana. *Boletín Geológico y Minero* **2007**, *118*, 221–242.
38. Torró, L.; García-Casco, A.; Proenza, J.A.; Blanco-Quintero, I.F.; Gutiérrez-Alonso, G.; Lewis, J.F. High-pressure greenschist to blueschist facies transition in the Maimón Formation (Dominican Republic) suggests mid-Cretaceous subduction of the Early Cretaceous Caribbean Arc. *Lithos* **2016**, *266–267*, 309–331. [[CrossRef](#)]
39. Lewis, J.F.; Astacio, V.A.; Espaillet, J.; Jiménez, J. The occurrence of volcanogenic massive sulfide deposits in the Maimón Formation, Dominican Republic: The Cerro de Maimón, Loma Pesada and Loma Barbuito deposits. In *VMS Deposits of Latin America*; Sherlock, R., Barsch, R., Logan, A., Eds.; Geological Society of Canada: Newfoundland, NL, Canada, 2000; Volume 2, pp. 213–239.
40. Torró, L.; Proenza, J.A.; Marchesi, C.; García-Casco, A.; Lewis, J.F. Petrogenesis of meta-volcanic rocks from the Maimón Formation (Dominican Republic): Geochemical record of the nascent Greater Antilles paleo-arc. *Lithos* **2017**, *278–281*, 255–273. [[CrossRef](#)]
41. Torró, L.; Proenza, J.A.; García-Casco, A.; Farré de Pablo, J.; del Carpio, R.; León, P.; Chávez, C.; Domínguez, H.; Brower, S.; Espaillet, J.; et al. La Geoquímica de la Formación Maimón (Cordillera Central, República Dominicana) revisada. *Boletín Geológico y Minero* **2017**, *128*, 517–539. (In Spanish) [[CrossRef](#)]
42. Torró, L.; Proenza, J.A.; Rojas-Agramonte, Y.; García-Casco, A.; Yang, J.-H.; Yang, Y.-H. Recycling in the subduction Factory: Archaean to Permian zircons in the oceanic Cretaceous Caribbean island-arc (Hispaniola). *Gondwana Res.* **2018**, *54*, 23–37. [[CrossRef](#)]

43. Kesler, S.; Russell, E.N.; Reyes, C.; Santos, L.; Rodriguez, A.; Fondeur, L. Geology of the Maimon Formation, Dominican Republic. In *Geologic and Tectonic Development of the North American: Caribbean Plate Boundary in Hispaniola*; Mann, P., Draper, G., Lewis, J.F., Eds.; Geological Society of America: Boulder, CO, USA, 1991; pp. 173–185.
44. Horan, S.L. The Geochemistry and Tectonic Significance of the Maimón-Amina Schists, Cordillera Central, Dominican Republic. Master's. Thesis, University of Florida, Gainesville, FL, USA, 1995.
45. Kesler, S.E.; Russell, N.; Polanco, J.; McCurdy, K.; Cumming, G.L. Geology and geochemistry of the early Cretaceous Los Ranchos Formation, central Dominican Republic. In *Geologic and Tectonic Development of the North American: Caribbean Plate Boundary in Hispaniola*; Mann, P., Draper, G., Lewis, J.F., Eds.; Geological Society of America: Boulder, CO, USA, 1991; pp. 187–201.
46. Escuder-Viruete, J.; Díaz de Neira, A.; Hernáiz Huerta, P.P.; Monthel, J.; García Senz, J.; Joubert, M.; Lopera, E.; Ullrich, T.; Friedman, R.; Mortensen, J.; et al. Magmatic relationships and ages of Caribbean island-arc tholeiites, boninites and related felsic rocks, Dominican Republic. *Lithos* **2006**, *90*, 161–186. [[CrossRef](#)]
47. Escuder-Viruete, J.; Contreras, F.; Stein, G.; Urien, P.; Joubert, M.; Pérez-Estaún, A.; Friedman, R.; Ullrich, T. Magmatic relationships and ages between adakites, magnesian andesites and Nb-enriched basalt-andesites from Hispaniola: Record of a major Change in the Caribbean island arc magma sources. *Lithos* **2007**, *99*, 151–177. [[CrossRef](#)]
48. Kesler, S.E.; Campbell, I.H.; Allen, C.M. Age of the Los Ranchos Formation, Dominican Republic: Timing and tectonic setting of primitive island arc volcanism in the Caribbean region. *Geol. Soc. Am. Bull.* **2005**, *117*, 987–995. [[CrossRef](#)]
49. Kesler, S.E.; Campbell, I.H.; Smith, C.N.; Hall, C.M.; Allen, C.M. Age of the Pueblo Viejo gold-silver deposit and its significance to models for high-sulfidation epithermal mineralizations. *Econ. Geol.* **2005**, *100*, 253–272. [[CrossRef](#)]
50. Martín, M.; Draper, G. *Mapa Geológico de la Hoja 6172-I (Hatillo), Scale 1:50,000 (SYSMIN, Proyecto C)*. Consorcio ITGE-PROINTEC-INYPSA; Dirección General de Minería: Santo Domingo, Dominican Republic, 1999.
51. Escuder-Viruete, J.; Pérez-Estaún, A.; Weis, D.; Friedman, R. Geochemical characteristics of the Río Verde Complex, Central Hispaniola: Implications for the paleotectonic reconstruction of the Lower Cretaceous Caribbean island-arc. *Lithos* **2010**, *114*, 168–185. [[CrossRef](#)]
52. Bowin, C.O. Geology of the central Dominican Republic. *Geol. Soc. Am. Mem.* **1966**, *98*, 11–84.
53. Lewis, J.F.; Amarante, A.; Bloise, G.; Jiménez, J.G.; Domínguez, H. Lithology and stratigraphy of the upper Cretaceous volcanic and volcanoclastic rocks of the Tiro Group, Dominican Republic, and correlations with the Massif du Nord in Haiti. In *Geologic and Tectonic Development of the North-America-Caribbean Plate Boundary in Española*; Mann, P., Draper, G., Lewis, J.F., Eds.; Geological Society of America: Boulder, CO, USA, 1991; pp. 143–163.
54. Bowin, C. The geology of Española. In *The Ocean Basins and Margins: The Gulf of Mexico and the Caribbean*; Naim, A., Stehli, F., Eds.; Plenum Press: New York, NY, USA, 1975; Volume 3, pp. 501–552.
55. Montgomery, H.; Pessagno, E.A. Cretaceous microfaunas of the Blue mountains, Jamaica, and of the Northern and Central Basement Complexes of Hispaniola. Caribbean Basins. In *Sedimentary Basins of the World*; Mann, P., Ed.; Elsevier Science B.V.: Amsterdam, The Netherlands, 1999; Volume 4, pp. 237–246.
56. McPhie, J.; Doyle, M.; Allen, R. *Volcanic Textures: A Guide to the Interpretation of Textures in Volcanic Rocks*; Centre for Ore Deposit and Exploration Studies, University of Tasmania: Hobart, Australia, 1993.
57. Pearce, J.A. Immobile elements fingerprinting of ophiolites. *Elements* **2014**, *10*, 101–108. [[CrossRef](#)]
58. Rojas-Agramonte, Y.; Garcia-Casco, A.; Kemp, A.; Króner, A.; Proenza, J.A.; Lázaro, C.; Liu, D. Recycling and transport of continental material through the mantle wedge above subduction zones: A Caribbean example. *Earth Planet. Sci. Lett.* **2016**, *436*, 93–107. [[CrossRef](#)]
59. Proenza, J.A.; González-Jiménez, J.M.; Garcia-Casco, A.; Belousova, E.; Griffin, W.L.; Talavera, C.; Rojas-Agramonte, Y.; Aiglsperger, T.; Navarro-Ciurana, D.; Pujol-Solà, N.; et al. Cold plumes trigger contamination of oceanic mantle wedges with continental crust-derived sediments: Evidence from chromitite zircon grains of eastern Cuban ophiolites. *Geosci. Front.* **2018**, in press. [[CrossRef](#)]
60. Tesfaye Firdu, F.; Taskinen, P. *Sulfide Mineralogy-Literature Review*; Aalto University Publications in Material Science and Engineering: Helsinki, Finland, 2010.

61. Keith, M.; Haase, K.M.; Schwarz-Schampera, U.; Klemd, R.; Petersen, S.; Bach, W. Effect of temperature, sulfur and oxygen fugacity on the composition of sphalerite from submarine hydrothermal vents. *Geology* **2014**, *42*, 699–702. [CrossRef]
62. Herzig, P.M. A Mineralogical, Geochemical and Thermal Profile Trough the Agrokipia “B” Hydrothermal Sulfide Deposit, Troodos Ophiolite Complex, Cyprus. In *Base Metal Sulfide Deposits*; Friedrich, G.H., Herzig, P.M., Eds.; Springer: Berlin, Germany, 1988; pp. 182–215.
63. Román-Alday, M.C.; Torró, L.; Proenza, J.A.; Melgarejo, J.C.; Romero, J.; Amarante, A.; Espaillet, J.; Nelson, C.E. The Romero Cu–Au–Zn Deposits, Cordillera Central, Dominican Republic: Preliminary data on the mineralogy and geochemistry of mineralization. In Proceedings of the 13th SGA Biennial Meeting, Nancy, France, 24–27 August 2015; Volume 5, pp. 2087–2090.
64. Sillitoe, R.H. Comments on Geology and Exploration of the Romero Gold-Copper Prospect and Environs, Las Tres Palmas Project, Dominican Republic. 2013. Available online: <https://www.goldquestcorp.com/images/pdf/RichardSillitoeReport-Jan2013.pdf> (accessed on 7 September 2018).
65. Tiroe Gold Trend. Available online: <https://www.precipitategold.com/projects/dominican-republic/tiroe-gold> (accessed on 7 September 2018).
66. Dominican Republic Projects, Goldquest. Available online: <https://www.goldquestcorp.com/index.php/projects> (accessed on 7 September 2018).
67. Simmons, S.F.; White, N.C.; John, D.A. Geological characteristics of epithermal precious and base metal deposits. *Econ. Geol.* **2005**, *100*, 485–522.
68. Shimizu, T. Reinterpretation of quartz textures in terms of hydrothermal fluid evolution at the Koryu Au–Ag deposit, Japan. *Econ. Geol.* **2014**, *109*, 2051–2065. [CrossRef]
69. Ogawa, Y.; Shikazono, N.; Ishiyama, D.; Sato, H.; Mizuta, T.; Nakano, T. Mechanism for anhydrite and gypsum formation in the Kuroko massive sulfide-sulfate deposits, North Japan. *Miner. Deposita* **2007**, *42*, 219–233. [CrossRef]
70. Paytan, A.; Kastner, M.; Campbell, D.; Thiemens, M.H. Seawater sulfur isotope fluctuations in the Cretaceous. *Science* **2004**, *304*, 1663–1665. [CrossRef] [PubMed]
71. Bottrell, S.H.; Newton, R.J. Reconstruction of changes in global sulfur cycling from marine sulfate isotopes. *Earth-Sci. Rev.* **2006**, *75*, 59–83. [CrossRef]
72. Sangster, D.F. Sulphur and lead isotopes in strata-bound deposits. In *Handbook of Strata-Bound and Stratiform Ore Deposits*; Wolf, K.H., Ed.; Elsevier: Amsterdam, The Netherlands, 1976; Volume 8, pp. 219–266.
73. Ohmoto, H. Stable isotope geochemistry of ore deposits. *Rev. Mineral. Geochem.* **1986**, *16*, 491–559.
74. Çagatay, M.N.; Eastoe, C.J. A sulfur isotope study of volcanogenic massive sulfide deposits of the eastern black sea province, Turkey. *Miner. Deposita* **1995**, *30*, 55–66. [CrossRef]
75. Ohmoto, H.; Goldhaber, M.B. Sulfur and carbon isotopes. In *Geochemistry of Hydrothermal ore Deposits*, 3rd ed.; Barnes, H.L., Ed.; John Wiley and Sons: New York, NY, USA, 1997; pp. 517–611, ISBN 978-0-471-57144-5.
76. Herzig, P.M.; Petersen, S.; Hannington, M.D. Geochemistry and sulfur isotopic composition of the TAG hydrothermal mound, Mid-Atlantic ridge, 26°N. *Proc. Ocean Drill. Program Sci. Results* **1998**, *158*, 47–68.
77. Amarante, A.; Jiménez, J.; Lewis, J.F. Geology, hydrothermal alteration and geochemistry of epithermal Au–Ag mineralization in the Restauración area Dominican Republic. In Proceedings of the Transactions 11th Caribbean Geological Conference, Bridgetown, Barbados, 20–26 July 1986.
78. Amarante, J.A.; Lewis, J.F. *Geological Setting and Characteristics of Base and Precious Metal Mineralization in the Cordillera Central of the Western Dominican Republic and Massif du Nord Haiti*; Abstracts with Programs; Geological Society of America: Boulder, CO, USA, 1996.
79. Lewis, W.J.; San Martin, A.J.; Gowans, R.M. NI 43-101 Technical Report Mineral Resource Estimate for the Candelones Extension Deposit, Candelones Project, Neita Concession, Dominican Republic; Micon International Limited: Toronto, ON, Canada, 2015; Available online: <http://www.unigoldinc.com/i/pdf/TechnicalReports/TechnicalReport-2015.pdf> (accessed on 9 September 2018).
80. Louca, K. Geological setting and base and precious metal deposits of Northern Haiti. In *Transactions of the 12th Caribbean Geological Conference, St. Croix, Virgin Islands, Puerto Rico*; Larue, D.K., Draper, G., Eds.; Miami Geological Society: Miami, FL, USA, 1990; pp. 200–216.

81. Stern, R.J.; Gerya, T. Subduction initiation in nature and models: A review. *Tectonophysics* **2017**. [[CrossRef](#)]
82. Whattam, S.A.; Stern, R.J. The “subduction initiation rule”: A key for linking ophiolites, intra-oceanic forearcs, and subduction initiation. *Contrib. Mineral. Petrol.* **2011**, *162*, 1031–1045. [[CrossRef](#)]



© 2018 by the authors. Licensee MDPI, Basel, Switzerland. This article is an open access article distributed under the terms and conditions of the Creative Commons Attribution (CC BY) license (<http://creativecommons.org/licenses/by/4.0/>).